Available online at www.sciencedirect.com
SCIENCE DIRECT®
Lithos 88 (2006) 150–172
LITHOS
www.elsevier.com/locate/lithos

A SHRIMP U–Pb and LA-ICP-MS trace element study of the petrogenesis of garnet–cordierite–orthoamphibole gneisses from the Central Zone of the Limpopo Belt, South Africa

Ian S. Buick [a,*], Jörg Hermann [b], Ian S. Williams [b], Roger L. Gibson [c], Daniela Rubatto [b]

[a] School of Geosciences, Monash University, Melbourne, Vic. 3800, Australia
[b] Research School of Earth Sciences (RSES), Australian National University, Canberra, A.C.T. 0200, Australia
[c] School of Geosciences, University of the Witwatersrand, Private Bag 3, WITS 2050, South Africa

Received 9 January 2005; accepted 27 June 2005
Available online 21 October 2005

Abstract

The Central Zone of the Limpopo Belt (South Africa) underwent high-grade metamorphism at ~2.7–2.5 and ~2.03 Ga. Quartz-rich, garnet-, cordierite-, biotite- and orthoamphibole-bearing, feldspar-free gneisses from the western Central Zone reached granulite-facies conditions (~800 °C at ~8–10 kbar) followed by decompression. Garnet from one such sample shows significant zonation in trace elements but little zonation in major elements. Zoning patterns suggest that the early prograde breakdown of REE-rich accessory phases contributed to the garnet trace element budget. Monazite from the sample yields a SHRIMP weighted mean ^{207}Pb–^{206}Pb age of 2028 ± 3 Ma, indistinguishable from a SHRIMP zircon age of 2022 ± 11 Ma previously measured on metamorphic overgrowths on ~2.69 Ga igneous zircon cores. New zircon and monazite formed before, or at, the metamorphic peak, and occur as inclusions in garnet. Monazite appears to have formed through the breakdown of early allanite ± xenotime ± apatite. Trace element zoning patterns in garnet and the age of accessory phases are most consistent with a single tectonometamorphic event at ~2.03 Ga.

The plagioclase and K-feldspar-free composition of the garnet–cordierite–orthoamphibole gneisses requires open system processes such as intense hydrothermal alteration of protoliths or advanced chemical weathering. In the studied sample, the ~2.69 Ga igneous zircons show a prominent negative Eu anomaly, suggesting equilibrium with plagioclase, or plagioclase fractionation in the precursor magma. In contrast, the other minerals either show small negative (~2.03 Ga monazite), no (~2.02 Ga zircon and garnet) or positive Eu anomalies (orthoamphibole). This suggests that the unusual bulk compositions of these rocks were set in after ~2.69 Ga but before the peak of the ~2.03 Ga event, most probably while the protoliths resided at shallow or surficial crustal levels.

Keywords: U–Pb age; LA-ICP-MS; REE; Alteration; Metamorphism; Limpopo Belt

1. Introduction

Constraining the timing of high-grade metamorphism is commonly difficult because age determinations that involve U–Pb geochronology of accessory phases (monazite, zircon, titanite, xenotime) need to be

* Corresponding author. Tel.: +61 3 99054892; fax: +61 3 99054903.
E-mail address: Ian.Buick@sci.monash.edu.au (I.S. Buick).

0024-4937/$ - see front matter © 2005 Elsevier B.V. All rights reserved.
doi:10.1016/j.lithos.2005.09.001

linked to pressure–temperature–time (P–T–t) paths through the growth/resorption of major P–T sensitive rock-forming minerals such as garnet. Making this link is non-trivial in high-grade rocks because accessory phases may: 1) pre-date and be unrelated to metamorphism (e.g., detrital zircon); 2) form during prograde metamorphic reactions involving other accessory phases and/or silicate minerals (Smith and Barreiro, 1990; Pyle and Spear, 2003; Kohn and Malloy, 2004); 3) form at the metamorphic peak (Pyle and Spear, 2003); 4) precipitate after the metamorphic peak, during the crystallisation of partial melt or exsolution of fluid at the solidus (Roberts and Finger, 1997); 5) form along the retrograde P–T–t path due to breakdown of major rock-forming minerals (Fraser et al., 1997; Degeling et al., 2001; Pyle and Spear, 2003); or 6) form due to solid state recrystallisation of pre-existing grains at any time during metamorphism (Hoskin and Black, 2000).

In addition, high-grade metamorphic terranes may have experienced more than one granulite-facies metamorphic event. Determining whether rocks have mono- or polycyclic high-grade histories is itself commonly difficult because major element compositional discontinuities that might indicate multiple garnet growth events are erased by volume diffusion at temperatures above ~700–750 °C (Tracy, 1982). In contrast, diffusion rates for trace elements, including the trivalent REE are commonly much slower than for major elements such as Fe and Mg in garnet (Van Orman et al., 2002), making it possible to use these tracers in garnet to determine growth histories in otherwise compositionally homogeneous grains (e.g., Pyle and Spear, 1999, 2003; Hermann and Rubatto, 2003). Integration of high-spatial resolution geochronology with the trace element chemistry of dated accessory phases and major rock-forming minerals provides a tool for better constraining the timing of high-grade (poly)metamorphism.

The Limpopo Belt of southern Africa (Fig. 1) is a terrain where the timing and distribution of polyphase granulite-facies metamorphism is uncertain. It comprises the Central Zone (CZ) and the flanking Southern and Northern Marginal Zones (SMZ and NMZ, respectively), which are separated by major ductile shear

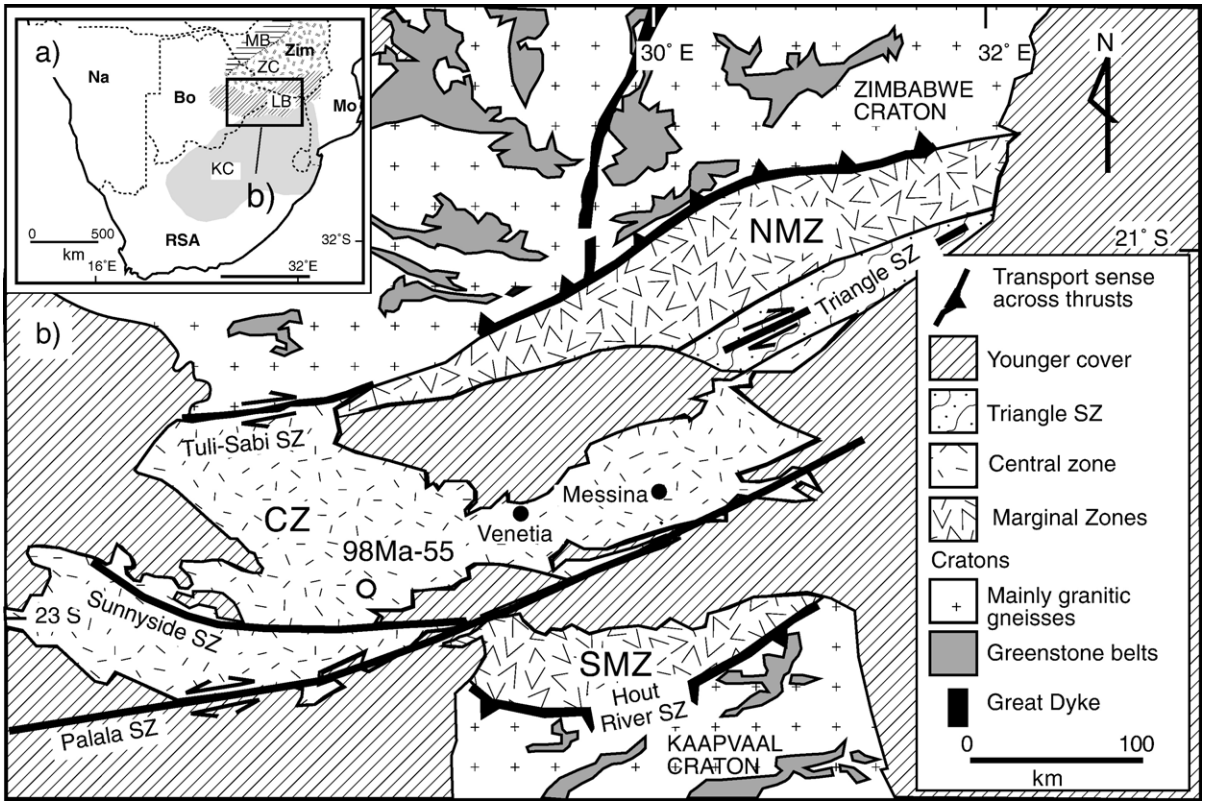

Fig. 1. a) Inset map showing the location of the Limpopo Belt and surrounding cratons; b) simplified geological map of the Limpopo Belt and adjacent Kaapvaal and Zimbabwe cratons. Abbreviations: Bo=Botswana; CZ=Central Zone; KC=Kaapvaal craton; LB=Limpopo Belt; MB=Magondi Belt; Mo=Mozambique; Na=Namibia; NMZ=Northern Marginal Zone; RSA=Republic of South Africa; SMZ=Southern Marginal Zone; SZ=shear zone; Zim=Zimbabwe; ZC=Zimbabwe craton. The location of sample 98 Ma-55 is shown by a white circle in b).

zones. Although there is general agreement that the rocks of the Northern and Southern Marginal Zones (Fig. 1) were thrust over their lower-grade equivalents on the adjacent cratons at ~2.7–2.6 Ga, debate continues about the absolute timing of thrusting and how the metamorphism, magmatism and deformation in the Central and Marginal Zones are related (Kröner et al., 1999). Models based on the predominance of ~2.7–2.5 Ga radiometric ages from "late-tectonic" granitoids in all three zones, and evidence of similar clockwise *P–T–t* paths in the Central Zone and Southern Marginal Zone regard the entire Limpopo Belt as a late Archaean orogenic zone formed during N–S collision of the Zimbabwe and Kaapvaal cratons (e.g., Roering et al., 1992). In contrast, other petrological and geochronological studies suggest that, although metamorphism occurred locally at ~2.7–2.5 Ga, the high-grade metamorphism (~8–12 kbar and ~800–850 °C; Watkeys, 1984; Holzer et al., 1998; Zeh et al., 2004) and subsequent high-temperature decompression that affected most of the Central Zone occurred at ~2.03–2.01 Ga (Kröner et al., 1998, 1999; Holzer et al., 1998; Buick et al., 2003).

This study revisits the locality of one of the Central Zone metasediments (Fig. 1) studied by Buick et al. (2003). It uses new SHRIMP U–Pb age determinations from metamorphic monazite, and mineral trace element analyses from coexisting monazite, zircon and major rock-forming minerals to show that these rocks most probably experienced only one high-grade event at ~2.03 Ga. Together, these data are used to constrain the timing of alteration processes that led to the development of the unusual feldspar-free bulk composition of this rock.

2. Geological setting

The Central Zone comprises metasediments (mainly quartzites, metapelites, metacarbonates), metabasites and a range of granitic gneisses whose plutonic protoliths were emplaced at ~3.3–3.1, ~2.7–2.5 and ~2.03 Ga (Kröner et al., 1998, 1999). In the interval ~2.7–2.5 Ga, more than one high-grade metamorphic event may have occurred in the Central Zone. Evidence for polymetamorphism is indicated by: 1) the occurrence of granulite-grade metapelitic xenoliths containing a foliation that is truncated by the surrounding ~2.60–2.57 Ga Bulai Batholith (Barton et al., 1994); and 2) a ~2.52 Ga garnet Pb stepped leach age obtained by Holzer et al. (1998) from a Central Zone granulite-facies metapelite. Protoliths to metasediments were originally inferred to have been deposited no later than ~3.2 Ga (Kröner et al., 1999). However, several studies have recently shown that the Central Zone additionally contains significantly younger (late Archaean to Palaeoproterozoic) supracrustal rocks (<~2.7 Ga, Buick et al., 2003; Barton et al., 2003).

Samples for this study were collected from a prominent ridge (Oom Stammetjie se Kop) on the farm Redbaan 78 MR, ~190 km west of Messina (Fig. 1). The local rocks form a sequence of intercalated garnet–cordierite–orthoamphibole–biotite ± orthopyroxene-bearing gneisses and garnet–cordierite quartzites, with minor biotite–sillimanite schists. Garnet-bearing metabasites also occur locally. Compositional layering strikes 130° and dips 20° to the NE; a mineral lineation defined by the preferred orientation of sillimanite and (locally) orthoamphibole plunges 15°/335°.

In addition to quartz, biotite, cordierite, zircon and monazite, which occur in all rock types, the following assemblages characterise the gneisses, schists and quartzites:

1) garnet – orthoamphibole ± orthopyroxene ± spinel ± sillimanite ± staurolite ± ilmentite ± rutile ± apatite (gneisses);
2) garnet ± plagioclase ± apatite or sillimanite ± apatite (schists);
3) garnet ± staurolite ± orthoamphibole (quartzites).

No samples contain K-feldspar, and plagioclase was observed in only one sample of garnet schist. In general, biotite defines a foliation and orthoamphibole, where present, occurs in centimetre diameter sprays of randomly oriented, prismatic grains within the foliation plane. Garnet in the gneisses and schists occurs as 5–15 mm diameter porphyroblasts that are wrapped by biotite. Staurolite is rare and occurs as inclusions in garnet or cordierite (after garnet). Garnet in the quartzites occurs as elongate mm-long porphyroblasts that are flattened within the fabric. In the gneisses and quartzites, cordierite also occurs as elongate, flattened polycrystalline aggregates aligned within the fabric. Unlike elsewhere in the Central Zone, none of the rocks show field evidence of partial melting.

3. Analytical methods

Monazite from sample 98 Ma-55 (RSES catalogue no. 99-005) was analysed for U–Th–Pb isotopes using the RSES SHRIMP II. A monazite concentrate was prepared by clean heavy liquid and magnetic separation techniques, then monazite grains were hand picked for

optical clarity and mounted in epoxy resin with reference monazite WB.T.329 (Thompson Mine, Manitoba; $^{206}Pb/^{238}U = 0.3152$; U = 2100 ppm). The mounts were polished and then individual grains were photographed in both reflected and transmitted light. Before analysis on SHRIMP II, the mount was coated with high-purity Au to prevent charging. A 2–4 nA, 10 kV O_2^- primary beam was focused to a 10–15 μm diameter spot on the target grains. Secondary ions were extracted at 10 kV, and analysed at a mass resolution of ~5000. Th, U and Pb isotopes of interest were measured on a single electron multiplier by cyclic stepping of the analyser magnetic field. Isotopic compositions were measured directly, without correction for mass fractionation (~0.25%/AMU). Inter-element Pb–U fractionation was corrected assuming a linear relationship between Pb^+/U^+ and $(UO^+/U^+)^2$ (Williams et al., 1996). Th–U fractionation was calculated from the slope of the $^{208}Pb/^{206}Pb$–ThO^+/UO^+ isochron (Williams et al., 1996). Analyses were corrected for laboratory-derived common Pb using ^{204}Pb and assuming a Broken Hill galena Pb isotopic composition. The count rate at mass 204 was corrected for a Th-related isobar by subtracting the count rate at ThO multiplied by 5.8×10^{-6}. All ages were calculated using the decay constants recommended by Steiger and Jäger (1977). Analytical uncertainties listed in the tables and plotted in the figures are one standard error precision estimates. Uncertainties in pooled ages, unless otherwise stated, are 95% confidence limits ($t\sigma$), and include the uncertainty in the analysis of the standard. Post-analysis back scattered electron (BSE) images of monazite were obtained with a Cambridge S360 scanning electron microscope using a voltage of 20 kV, a current of ~3 nA and a working distance of ~20 mm. Analytical methods, cathodoluminescence imagery and U–Pb–Th isotopic data obtained from a grain mount of zircon from the same sample are described in Buick et al. (2003).

Major element analysis of minerals (WDS) in polished thin sections was carried out at the University of Melbourne on a Cameca SX50 electron microprobe. Analytical conditions were 15 kV and 25 nA, and data were reduced using Cameca PAP matrix corrections. BSE images of textural relationships between accessory phases and major silicate minerals were taken on a Phillips XL30 electron microscope (20 kv, 2 nA; University of Melbourne) and the phases identified using EDS. Trace element analyses of the same minerals in situ were performed on the Laser Ablation (LA) ICP-MS at the RSES. A pulsed 193 nm ArF Excimer laser with 100 mJ energy at a repetition rate of 5 Hz coupled to an Agilent 7500 quadrupole ICP-MS was used for ablation. Si and Ca contents determined by electron microprobe were used as internal standards for silicate minerals. During the time-resolved analysis of minerals, possible contamination from inclusions and fractures were detected by monitoring several elements and integrating only the 'clean' part of the signal. A spot size of 86–112 μm was used for most minerals. NIST-612 glass was used as the external standard, assuming the composition given by Pearce et al. (1997). A BCR-2G glass was used as secondary standard. The average of six analyses of this glass yielded trace element contents that were typically within 2–6% of the certified values for this standard. Reproducibility about the mean values were between 0.5% and 4% relative (1σ), and <2% relative for the majority of elements. Precision of individual LA-ICP-MS spot analyses is typically 5–10% relative (cf. Košler, 2001). Trace element concentrations were also determined from the monazite in the SHRIMP epoxy mount (this study) and zircon from the epoxy mount of Buick et al. (2003) by ablating the same spots previously analysed by SHRIMP II using a spot size of 19–24 μm (zircon) and 32 μm (monazite). Additional trace element data were determined in thin section from monazite inclusions within garnet. Si and Ce were used as internal standards for zircon and monazite, respectively.

Powders for bulk rock analyses were prepared by grinding the sample in a tungsten carbide mill to a grain size of <25 μm. These were fused into glass discs using a La_2O_3-doped lithium-borate flux (0.84 g of sample to 4.5 g of flux), and the major elements analysed on the Siemens SRS303AS XRF spectrometer with a Rh end window X-ray tube at La Trobe University. The same rock powders were used for trace element whole-rock determinations. These powders were made into fused glass discs using a REE-free lithium-borate (Sigma® 12:22 X-Ray flux; sample:flux = 1:2) at the University of Stellenbosch, South Africa. They were then analysed for trace elements on the RSES LA-ICP-MS facility using a 142 μm spot size, with the resulting data being an average of 4 ablation spots. The relative 1 standard deviation of quadruplicate glass analyses is ~0.5–5% relative to average concentrations (~0.5–2% relative for most samples and elements), similar to the reproducibility of the BCR-2G secondary standard.

4. Results

4.1. Whole rock geochemistry

The whole rock major, trace and rare earth element (REE) compositions of seventeen samples from the Oom Stammetjie se Kop locality taken over an across

Table 1
Major and trace element data for bulk rock samples from the Oom Stammetjies se Kop locality

Sample	98 Ma-36A	98 Ma-36B	98 Ma-37	98 Ma-38	98 Ma-39	98 Ma-41	98 Ma-43	98 Ma-44	98 Ma-46	98 Ma-52	98 Ma-54	98 Ma-55	Lim-49	Lim-51	Lim-54	Lim-50A	Lim-53
Major elements (wt.%)																	
SiO_2	42.33	73.61	50.36	58.31	57.98	64.34	61.26	69.72	51.96	63.62	55.77	74.19	57.72	78.39	74.44	78.27	83.07
TiO_2	1.79	0.36	2.45	1.34	1.39	0.96	1.42	0.60	1.43	1.08	1.86	0.65	1.43	0.44	0.36	0.43	0.38
Al_2O_3	22.23	11.69	14.57	12.64	13.91	13.22	12.30	11.54	14.45	11.43	14.13	10.34	11.25	8.26	11.31	8.36	6.84
Fe_2O_{3tot}	15.80	6.68	18.13	17.08	17.03	11.86	17.29	8.33	19.24	11.37	15.75	9.72	12.62	7.52	6.30	7.69	5.28
MnO	0.14	0.02	0.15	0.15	0.15	0.23	0.11	0.05	0.22	0.12	0.17	0.08	0.12	0.07	0.07	0.06	0.06
MgO	12.65	6.02	12.22	9.44	8.92	3.16	7.00	4.22	11.73	6.93	10.29	4.78	10.49	3.86	3.85	3.76	2.64
CaO	0.33	0.12	0.96	0.61	0.32	3.78	0.75	0.06	0.34	0.36	1.46	0.23	0.51	0.10	0.12	0.10	0.09
Na_2O	0.51	0.20	0.54	0.28	0.19	0.46	0.27	0.13	0.46	0.25	0.42	0.05	0.00	0.07	0.05	0.08	0.08
K_2O	3.14	1.06	0.81	0.46	0.65	1.78	0.78	3.63	0.44	4.46	0.76	0.94	0.23	1.08	2.41	0.98	1.07
P_2O_5	0.12	0.03	0.43	0.08	0.15	0.19	0.29	0.06	0.16	0.17	0.58	0.07	0.28	0.05	0.03	0.07	0.05
LOI	2.23	1.71	0.85	0.77	0.85	1.55	0.00	2.23	1.31	1.23	0.48	0.63	5.68	0.69	1.57	0.62	0.82
Total	101.27	101.50	101.47	101.16	101.54	101.53	101.47	100.57	101.74	101.02	101.67	101.68	100.33	100.53	100.51	100.42	100.38
Trace elements (ppm)																	
Sc	38	13	42	29	39	24	42	15	34	26	31	35	30	12	7.0	13	25
V	296	171	315	301	284	232	278	160	300	242	321	302	241	91	34	87	171
Cr	329	142	160	120	122	1631	444	960	107	254	216	148	76	19	18	19	24
Cu	13	10	7.1	27	3.9	16	12	5.5	12	5.5	19	12	5.6	5.6	12	5.2	15
Zn	133	82	118	82	57	47	45	65	148	72	114	106	82	44	47	39	65
Ga	58	26	21	25	25	32	20	46	20	44	25	23	23	27	45	25	40
Rb	82	29	23	12	18	40	19	117	11	94	19	16	15	34	88	32	38
Sr	7.2	4.6	7.5	4.1	3.9	55.6	4.8	2.9	4.4	6.6	7.4	5.2	9.2	4.7	2.9	4.5	7.1
Y	103	117	55	181	285	101	57	108	55	87	41	127	69	148	103	149	220
Zr	434	468	237	225	193	456	213	511	235	397	238	222	255	322	518	331	390
Nb	55	14	15	17	19	29	14	27	19	23	13	17	17	23	30	23	28
Cs	0.95	0.79	0.31	0.24	0.31	0.29	0.23	0.86	0.30	0.95	0.21	0.27	0.17	0.32	0.60	0.24	0.31
Ba	348	81	54	29	71	341	90	646	68	696	83	74	15	191	564	175	295
La	108	108	40	53	541	60	11	80	48	66	83	224	152	277	67	666	574
Ce	217	219	65	112	930	118	18	161	98	128	62	363	84	432	136	421	794
Pr	24	24	8.0	13	89	14	2.3	18	11	15	7.5	36	11	46	16	45	82
Nd	99	97	35	53	328	58	10	73	46	62	32	135	42	170	64	166	300
Sm	21	21	8.7	14	56	14	3.2	15	10	13	7.9	25	10	31	14	31	50
Eu	2.8	2.9	1.7	2.4	9.3	2.3	1.1	2.5	1.9	2.7	2.3	4.5	1.8	6.3	2.2	6.3	11
Gd	20	22	10	23	51	16	6.3	15	10	15	9.2	23	12	35	17	39	52
Tb	3.0	3.4	1.7	4.3	6.7	2.6	1.3	2.5	1.5	2.3	1.4	3.2	1.8	4.3	2.7	4.2	5.9
Dy	19	21	11	29	42	18	10	18	10	16	8.1	20	12	26	19	25	36
Ho	3.9	4.3	1.9	5.7	8.0	3.9	2.1	4.2	2.0	3.4	1.5	3.8	2.6	4.9	4.0	4.8	6.8
Er	11	12	5.2	15	21	12	6.4	13	6.5	10	4.1	11	7.9	13	12	13	19
Tm	1.7	1.7	0.7	2.0	2.7	1.8	0.94	2.0	0.97	1.6	0.59	1.4	1.2	1.8	1.8	1.8	2.6
Yb	12	11	5.0	12	16	12	6.3	14	6.6	11	4.0	9.0	7.9	12	12	12	17
Lu	1.8	1.6	0.75	1.7	2.0	1.7	0.94	2.1	1.0	1.6	0.59	1.2	1.2	1.7	1.8	1.7	2.4
Hf	12	13	6.2	6.2	5.5	14	7.1	16	6.4	12	5.7	5.9	7.0	9.6	15	9.7	11
Th	25	28	7.1	13	11	26	11	23	12	21	5.6	9.6	15	21	30	20	25
U	7.3	8.0	4.1	4.3	3.7	6.8	2.8	4.1	3.4	4.2	3.0	3.4	3.1	5.1	6.1	5.0	6.3
Eu/Eu*	0.41	0.41	0.54	0.40	0.53	0.47	0.74	0.49	0.60	0.58	0.82	0.57	0.49	0.59	0.44	0.56	0.67

strike distance of ~75–100 m are given in Table 1 and Figs. 2 and 3. The samples include quartz-bearing orthoamphibole-rich gneisses (98 Ma-36A, -37, -38, -39, -43, -46, -54; Lim-49) that have low to moderate SiO_2 contents (~42–64 wt.%), and more silica-rich (~72–83 wt.% SiO_2) garnet–cordierite–biotite-bearing

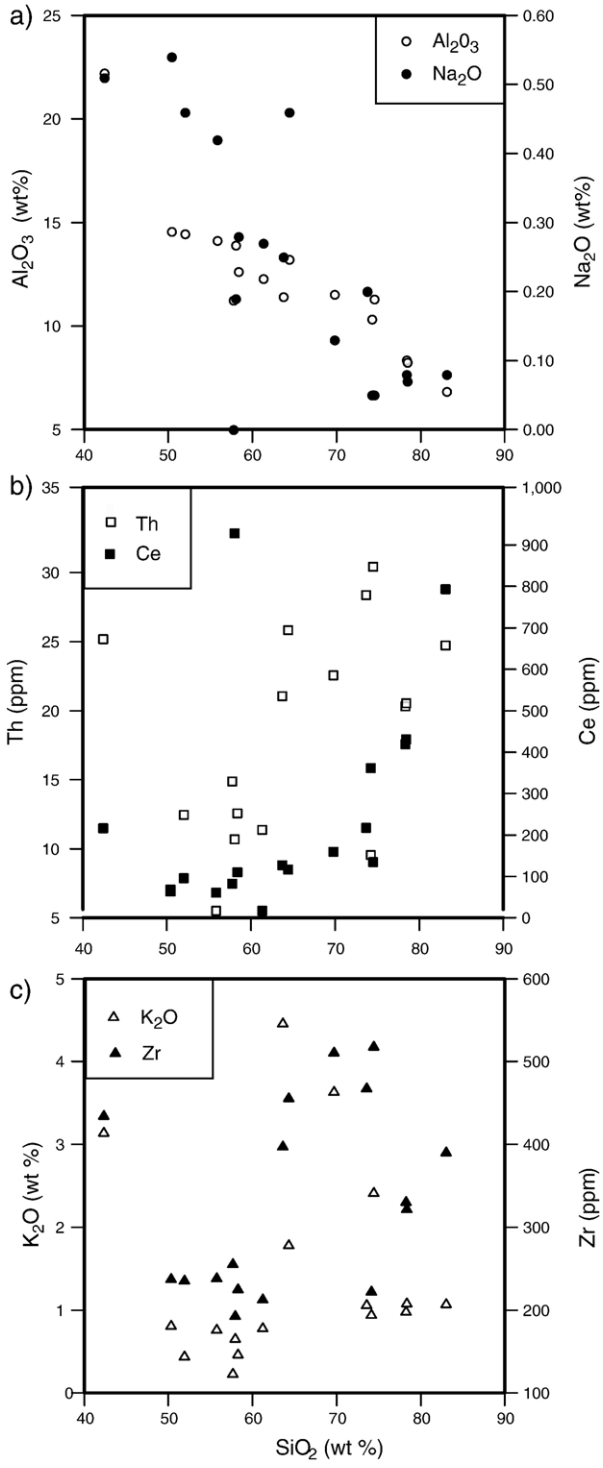

Fig. 2. Geochemical trends as a function of SiO_2 content for selected major and trace elements for whole rock samples from the Oom Stammetjie se Kop locality.

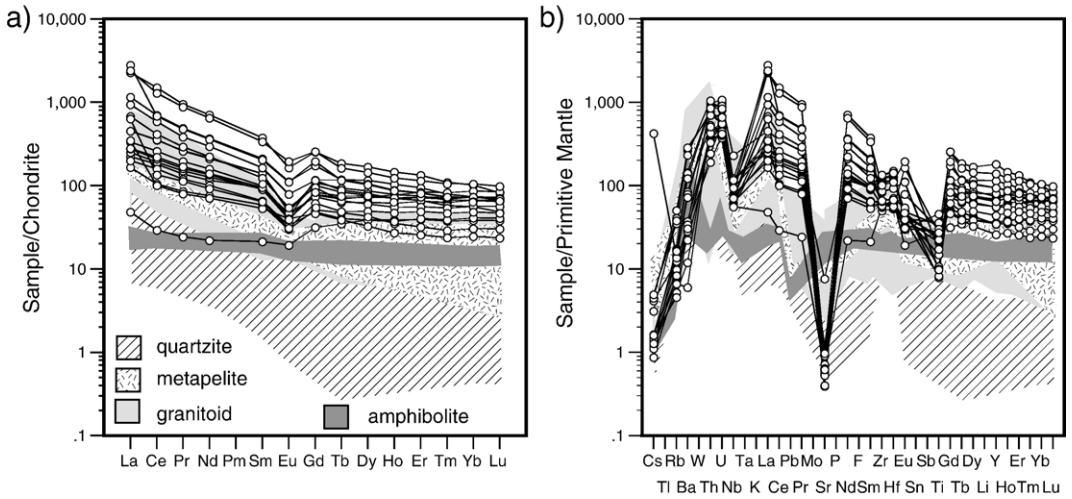

Fig. 3. a) Chondrite-normalised (Sun and McDonough, 1989) whole rock REE data from Oom Stammetjie se Kop; and b) primitive mantle-normalised (McDonough and Sun, 1995) spider plot for whole rock samples from Oom Stammetjie se Kop, compared with the data for different rock types from the Central Zone (Boryta and Condie, 1990).

gneisses and quartzites that additionally contain minor orthoamphibole (98 Ma-36b, -55; LIM-50A, -51, -53, -54). None contain plagioclase or K-feldspar (although sample 98 Ma-55 was incorrectly described as containing plagioclase by Buick et al., 2003). In addition, a single gneiss containing biotite, garnet and plagioclase (98 Ma-41), and a feldspar- and garnet-free, biotite–sillimanite-rich schist (98 Ma-52) were also sampled. With increasing SiO_2 there is generally a decrease in Al_2O_3, TiO_2, MnO, MgO, $Fe_2O_3(Fe_{Tot})$, Na_2O, Sc, V, Cu and Zn, and an increase in Y, Th and REE (Fig. 2a,b). Zr, K_2O (Fig. 2c), Hf, Rb, Ba and Cr occur in highest concentrations in samples with ~65–75 wt.% SiO_2. Chondrite-normalised REE patterns (Fig. 3a; Sun and McDonough, 1989) are characterised by moderate enrichment in LREE (La_N/Gd_N=1.5–14.4; mostly >3) moderate to small negative Eu anomalies ($Eu/Eu^*=Eu_N/((Sm_N.Gd_N)0.5)$=0.40–0.82), and somewhat flatter trends in the middle to heavy REEs (Gd_N/Lu_N=0.8–3.1). Overall, the LREE are significantly enriched (La_N as high as ~3000) compared to the REE compositions of other rock types from the Central Zone (Boryta and Condie, 1990; Fig. 3a). On a primitive mantle-normalised trace element diagram (Fig. 3b; McDonough and Sun, 1995) the studied rocks are characterised by anomalously low Sr contents that overlap only those of almost pure Central Zone quartzites (~90–97 wt.% SiO_2; Boryta and Condie, 1990). The most striking features of the data are the abnormally low contents of CaO, Na_2O, Sr and, to a lesser extent K_2O, and the enrichment in REE (in particular, the L-MREE). The low CaO, Na_2O and Sr contents are consistent with the lack of plagioclase feldspar in almost all samples.

In the following sections we present mineral major and trace element geochemistry, and SHRIMP U–Th–Pb geochronology from one of the more silica-rich samples (98 Ma-55: SiO_2=74.2 wt.%; La_N=945; La_N/Gd_N=8.1; Eu/Eu^*=0.57; Gd_N/Lu_N=2.4) from this locality, in order to explore how such bulk compositions may develop.

4.2. Petrography

Sample 98 Ma-55, which was also studied by Buick et al. (2003), is a strongly foliated, leucocratic gneiss (Fig. 4) containing abundant quartz, garnet, cordierite and biotite, subordinate sillimanite, spinel and orthoamphibole, and rutile, ilmenite, monazite, zircon, allanite and staurolite as accessories. It was collected near the base of the ridge, where it is interlayered with quartzite. In thin section, garnet porphyroblasts are wrapped by a biotite foliation. Garnet grains are locally poikiloblastic in their cores. They contain rare inclusions of staurolite (Fig. 5a) and biotite, as well as abundant inclusions of quartz, ilmenite and rutile, all of which also occur in the matrix. Orthoamphibole is a minor constituent, and is intergrown with biotite in the foliation (Fig. 5b). Cordierite occurs as flattened and internally annealed composite grain aggregates that are aligned with the biotite foliation. It contains relict prismatic sillimanite and newly-formed, vermicular spinel and ilmenite (Fig. 5c). Garnet is partially embayed by biotite, and by vermicular cordierite–quartz intergrowths (Fig. 5d).

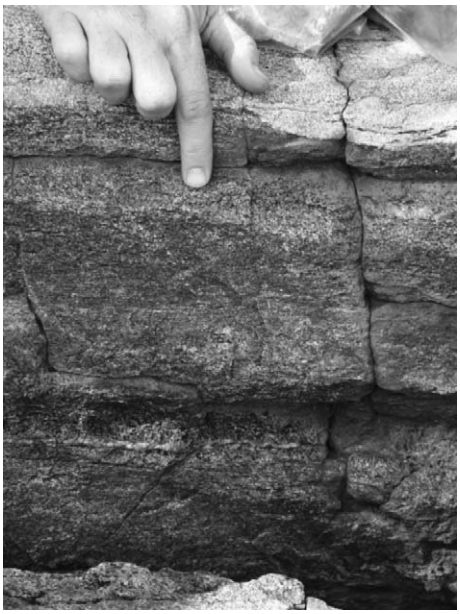

Fig. 4. Field photograph of well layered, quartz-rich, feldspar-absent, garnet–cordierite–biotite–sillimanite–orthoamphibole-bearing gneiss from the Oom Stammetjie se Kop locality where sample 98 Ma-55 was obtained.

Rutile, ilmenite, monazite and zircon occur in the rock matrix, and also as inclusions in garnet. Together with quartz, they commonly occur as inclusion trails (Fig. 6a) in garnet. The inclusion trails are oriented subparallel to the external biotite fabric. Both the monazite and zircon inclusions occur at a range of grain sizes from 2–5 up to 100 μm. The smallest grains commonly form composite clusters, sometimes elongate within the inclusion trace, and the zircons in these do not show visible internal zoning (Fig. 6b). The larger zircon inclusions commonly consist of a euhedral core > 50 μm diameter surrounded by an irregular, 5–15 μm wide overgrowth (Fig. 6c). The zircon overgrowths locally contain micron-sized inclusions of monazite (Fig. 6c), and monazite locally also contains micro-inclusions of zircon. Zircon and monazite are not uniformly distributed in the garnet. They tend to concentrate in discrete zones; however, they are both distributed at lower abundance throughout most of the garnet, except for garnet cores. Metamict allanite was found in the cores of several garnet grains; its grain boundaries are locally decorated by very small monazite grains (Fig. 6d).

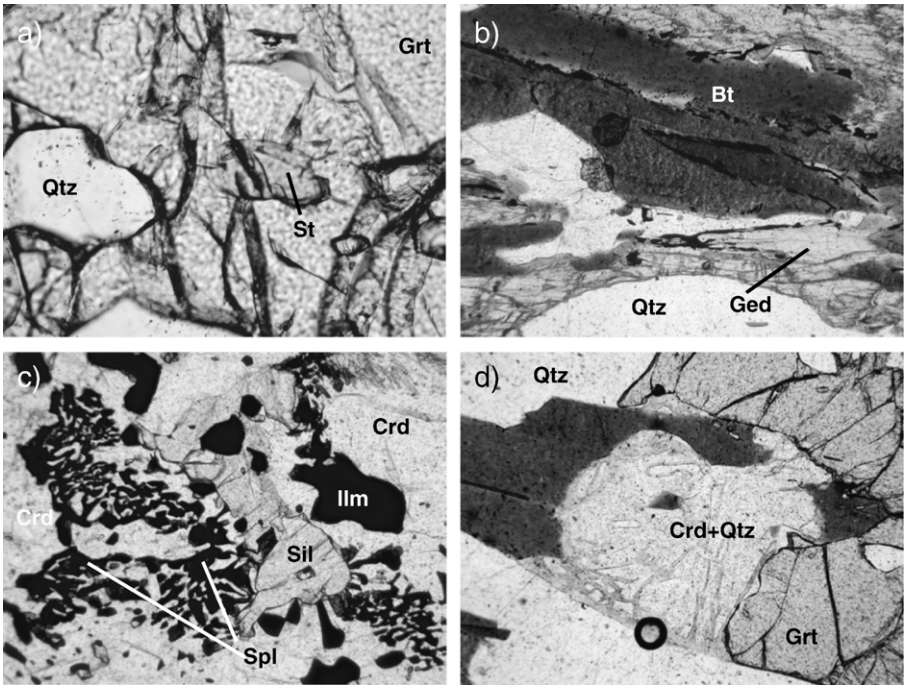

Fig. 5. Photomicrographs (plane polarized light) of textures from 98 Ma-55. a) An inclusion of staurolite (St) within garnet (Grt); b) intergrown gedrite (Ged) and biotite (Bt) define a foliation that wraps garnet; c) relict prismatic sillimanite (Sil) surrounded by spinel (Spl) and ilmenite (Ilm) within an aggregate of polygonal cordierite (Crd); d) garnet partially embayed by biotite and cordierite + quartz. The bold circle in the bottom of the view is a bubble. Width of the field of view = 1.3 mm (a) and 3 mm (b–d).

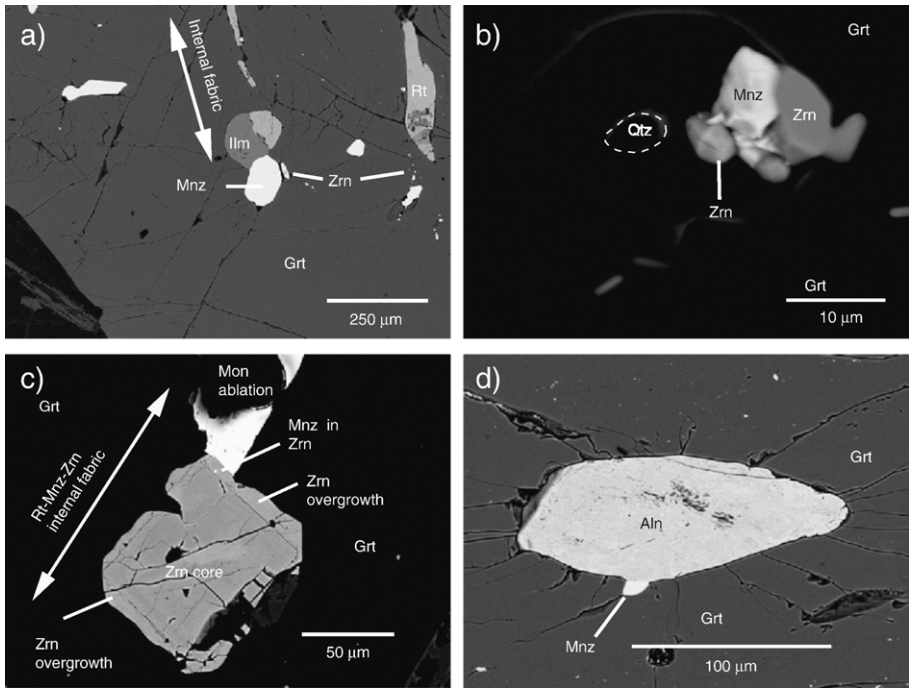

Fig. 6. BSE images of textures involving U–Pb accessory phases in thin section: a) oriented inclusion trails of rutile (Rt), ilmenite (Ilm), monazite (Mnz) and zircon (Zrn) in garnet (Grt); b) a cluster of fine-grained monazite and zircon included in garnet; c) a composite coarse-grained zircon inclusion in garnet, comprising a euhedral core and narrow irregular overgrowth. The overgrowth contains a micron-sized monazite inclusion; d) metamict allanite (Aln) included in garnet, surrounded by radial hydration cracks and decorated with a small monazite grain. The contrast and brightness of images has been manipulated and is not constant from one image to the next.

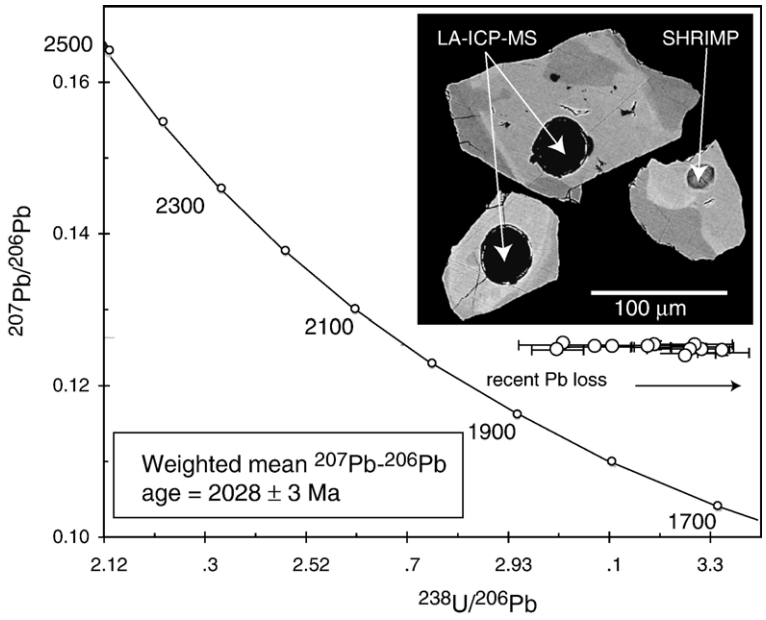

Fig. 7. Tera–Wasserburg concordia diagram showing SHRIMP analyses of monazite from a grain mount from sample 98 Ma-55. The inset shows a post-analysis BSE image of monazite and ablation pits for SHRIMP and LA-ICP-MS analysis. The two ~32 μm LA-ICP-MS pits also sit on top of SHRIMP analysis spots.

4.3. SHRIMP U–Pb geochronology

Monazite grains in the epoxy mount from 98 Ma-55 are clear and honey yellow, equant to slightly elongate, rounded and up to 150–200 μm in diameter. Fractures are relatively uncommon; micro-inclusions of zircon occur locally. BSE images show that most monazite grains are characterised by an irregular brighter core region and darker rims (Fig. 7). Some smaller grains are either BSE-bright or dark. Most, but not all, SHRIMP analyses were obtained from the BSE-bright core regions; however no difference in apparent age was found as a function of BSE response. The monazite grains have a range of U and Th contents (940–2400 and 1440–13700 ppm, respectively), and low to moderate Th/U (1.28–9.23; Table 2). Their isotopic compositions are plotted on a Tera–Wasserburg concordia diagram in Fig. 7. The data are normally discordant but $^{207}Pb/^{206}Pb$ is constant, indicative of recent Pb loss. The weighted mean $^{207}Pb/^{206}Pb$ (0.12494 ± 0.00022) is equivalent to an age of 2028 ± 3 Ma ($t\sigma$).

SHRIMP U–Pb analyses of zircon from the same sample (Buick et al., 2003) are plotted in Fig. 8. Zircon occurs as coarse 50–200 μm diameter, stubby, subhedral prismatic grains. CL imagery reveals that most grains are in whole or in part strongly euhedrally zoned (Fig. 8a), consistent with an origin from a felsic igneous protolith. Some grains have thin (<10–20 μm), irregular, typically weakly luminescent overgrowths (Fig. 8a). Similar, finely zoned cores and weakly luminescent overgrowths occur in zircon included in garnet (Fig. 8b). The euhedrally zoned zircon cores in the grain mount locally contain inclusions of quartz and apatite. They define a single, near-concordant population with a weighted mean $^{207}Pb/^{206}Pb$ age of 2692 ± 8 ($t\sigma$) Ma (Buick et al., 2003) and have moderate Th/U (0.39–0.56), consistent with an igneous origin (Williams and Claesson, 1987). In contrast, the overgrowths have low Th/U and yielded two different ages; the majority, with Th/U<0.04, plot in a near-concordant cluster with evidence of early Pb loss; the most concordant of these yielded a weighted mean $^{207}Pb/^{206}Pb$ age of 2022 ± 11 ($t\sigma$) Ma (Buick et al., 2003), within error of that obtained from monazite. Two overgrowth analyses (Th/U=0.09 and 0.11) gave near-concordant ages of ~2.2 Ga (Fig. 8; see Fig. 5c of Buick et al., 2003). The low Th/U and lack of pronounced growth structure in the ~2.02 Ga overgrowths are consistent with their being of metamorphic origin (Williams and Claesson, 1987). Although the location of the ~2.2 Ga SHRIMP analysis spots suggests that they did not overlap a boundary between ~2.69 and ~2.02 Ga zir-

Table 2
SHRIMP U–Th–Pb data from monazite from sample 98 Ma-55

Sample	U (ppm)	Th (ppm)	Pb* (ppm)	Th/U	$^{204}Pb/^{206}Pb$	±	% ^{206}Pb com	$^{208}Pb/^{206}Pb$	±	$^{208}Pb/^{232}Th$	±	$^{206}Pb/^{238}U$	±	$^{207}Pb/^{235}U$	±	$^{207}Pb/^{206}Pb$	±	Apparent age (Ma) $^{208}Pb/^{232}Th$	±	$^{206}Pb/^{238}U$	±	$^{207}Pb/^{235}U$	±	$^{207}Pb/^{206}Pb$	±
Grain																									
1.1	1027	3325	611	3.24	0.000003	3	0.004	0.925	3	0.0953	18	0.3336	57	5.74	10	0.12471	37	1841	33	1856	27	1937	15	2025	5
2.1	2221	10,557	1555	4.75	0.000003	2	0.005	1.347	4	0.0922	24	0.3254	80	5.61	14	0.12512	34	1783	45	1816	39	1918	22	2030	5
3.1	2096	4127	959	1.97	0.000001	1	0.001	0.551	3	0.0879	13	0.3142	40	5.42	7	0.12505	40	1702	24	1762	20	1888	12	2030	6
4.1	2423	13,681	1828	5.65	0.000012	4	0.018	1.566	4	0.0893	11	0.3219	39	5.56	7	0.12515	31	1729	21	1799	19	1909	11	2031	4
5.1	1487	7378	985	4.96	0.000005	4	0.008	1.355	3	0.0838	22	0.3071	77	5.29	13	0.12484	36	1627	42	1726	38	1867	22	2027	5
6.1	950	2435	441	2.56	0.000010	1	0.015	0.697	4	0.0797	23	0.2930	77	5.04	14	0.12462	53	1549	42	1657	38	1825	23	2023	8
7.1	1224	11,289	1224	9.23	0.000010	4	0.016	2.541	8	0.0862	25	0.3131	84	5.41	15	0.12533	59	1672	46	1756	41	1886	24	2033	8
8.1	1173	5290	709	4.51	0.000010	1	0.015	1.186	5	0.0791	13	0.3007	46	5.16	8	0.12436	37	1538	25	1695	23	1845	14	2020	5
9.1	943	4053	575	4.30	0.000013	8	0.019	1.156	4	0.0827	15	0.3072	52	5.26	9	0.12423	38	1606	28	1727	26	1863	15	2018	5
10.1	1122	8217	934	7.32	0.000006	4	0.009	2.013	8	0.0837	17	0.3046	58	5.26	10	0.12513	43	1625	32	1714	29	1862	17	2031	6
11.1	1356	4592	820	3.39	0.000008	3	0.012	0.968	2	0.0949	31	0.3320	101	5.74	18	0.12537	32	1833	57	1848	49	1937	27	2034	5
12.1	1120	1438	442	1.28	0.000005	2	0.008	0.363	2	0.0864	22	0.3059	70	5.29	13	0.12546	56	1675	40	1720	35	1867	21	2035	8

Pb*=radiogenic Pb.
% ^{206} Pb com=% common Pb.
Uncertainties are 1σ.

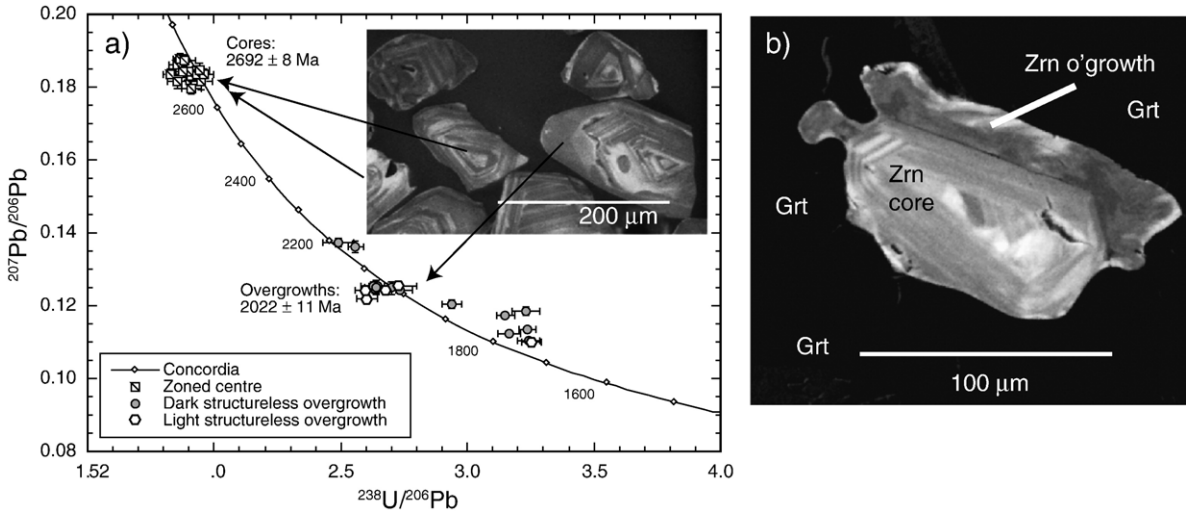

Fig. 8. a) Tera–Wasserburg concordia diagram showing SHRIMP analyses of zircon from sample 98 Ma-55 modified after Buick et al. (2003). The inset shows a cathodoluminescence image of zircon with a ~2.69 Ga moderate Th/U core and ~2.02 Ga low Th/U overgrowth; b) CL image of zircon inclusion in garnet (98 Ma-55), showing similar, finely zoned cores and narrow, CL-dark overgrowths.

con, trace element data and regional geochronological constraints (discussed below) are consistent with them representing a mixed age.

4.4. Mineral major element chemistry

Major element mineral compositions are summarized in Table 3. *Garnet* is an almandine–pyrope solid solution with very low grossular and spessartine contents ($Alm_{62–74}Prp_{23–35}Grs_{1.5–2}5Sps_{0.5–1.0}$). Fig. 9a shows the major element core to rim zonation across one garnet grain whose rim was contact only with matrix quartz. The traverse was chosen to minimize the effects of post-peak exchange/resorption on trace element compositions. Along it the garnet shows little major element compositional zonation from core to rim; X_{Mg} (Mg/Mg+Fe) varies from 0.37 to 0.35, grossular decreases irregularly from 2.5 to 1.5 mol% from cores to within ~100 µm of rims; spessartine also shows an small initial rimwards decrease followed by slight enrichment within ~100 µm of the grain rims. Enrichment of Mn is more pronounced, and significant lowering of X_{Mg} occurs (to X_{Mg} as low as 0.24–0.28), at rims in other grains where garnet is partially embayed by cordierite and/or biotite (not further considered here). *Cordierite* in the matrix has X_{Mg}=0.74–0.76 and very low alkali contents (Na+K=0.01–0.03 cations per 18 oxygen formula unit); the latter is consistent with the low alkali content of the bulk rock. *Biotite* has moderate Ti contents (0.19–0.22 cations per 11 oxygen formula unit), X_{Mg} between 0.63 and 0.65, and is also somewhat alkali depleted (K+Na=0.86–0.88 cations per 11 oxygen formula unit). The alkali deficiency may reflect the unusual bulk rock composition or incipient chloritisation; however the latter was not observed in thin section. The *orthoamphibole* has X_{Mg}=0.54–0.57 and is gedrite (Si=6.77–6.97 cations per 23 oxygen formula unit) according to the classification scheme of Leake et al. (1997). *Staurolite* inclusions in garnet have relatively low X_{Mg} (0.34–0.35) and Zn contents (0.30–0.48 wt.%; 0.03–0.05 cations per 23 oxygen formula unit). *Spinel* included within cordierite has X_{Mg}=0.26–0.27 and contains ~5 mol% of the magnetite end member. *Ilmenite* intergrown with spinel within polycrystalline cordierite contains ~10–14 mol% of the hematite end member (Fe^{3+} calculated by charge balance) and has X_{Mg}=0.002–003.

4.5. Trace element geochemistry of accessory and major phases

Monazite from the SHRIMP grain mount is characterised by moderate lowering of chondrite-normalised abundances from the LREE to MREE (La_N/Gd_N=7.2–9.4), a small negative Eu anomaly (Eu/Eu*=0.74–0.81) and steep fall in normalised abundance from the MREE to the HREE (Gd_N/Lu_N=152–869; Fig. 10). Y contents and Th/U are in the ranges ~14,000–23,000 ppm and 2.3–8.7, respectively (Table 4). Monazite analysed in thin section as inclusions within garnet has a narrower range of trace element contents (Y=~13,000–15,000 ppm; Th/U=1.98–3.81) and REE patterns (Eu/Eu*=0.81–0.85; La_N/Gd_N=8.0–8.4; Gd_N/Lu_N=212–252; Table 4) but overlaps those obtained

Table 3
Representative major (electron microprobe) element data for major silicate minerals from sample 98 Ma-55

	Grt core	Grt mid	Grt near rim	Grt rim	Ged matrix	Ged matrix	Bt matrix	Bt matrix	Crd matrix	Crd matrix	St inclusion	St inclusion	Spl in Crd	Spl in Crd	Ilm in Crd	Ilm in Crd
SiO_2	38.96	39.27	38.92	38.84	47.47	46.67	38.52	37.60	50.11	50.60	25.74	26.00	0.04	0.02	0.01	0.16
TiO_2	0.00	0.01	0.00	0.00	0.25	0.41	3.42	3.44	0.01	0.02	1.02	1.03	–	0.01	48.76	49.38
Al_2O_3	21.79	21.80	21.78	21.51	11.35	12.20	15.77	15.58	33.48	33.76	55.88	55.86	56.92	56.32	0.01	0.18
FeO	29.89	29.53	29.67	29.53	22.74	22.25	14.61	14.22	6.02	5.93	11.52	11.71	35.20	35.80	49.48	48.05
MnO	0.30	0.29	0.28	0.35	0.14	0.08	0.02	0.06	0.08	0.05	–	–	0.03	0.02	0.13	0.15
MgO	9.13	9.07	9.02	8.94	15.08	15.11	14.73	14.55	10.16	10.10	3.55	3.54	6.25	6.02	0.50	0.65
CaO	0.84	0.58	0.59	0.65	0.39	0.45	0.00	0.06	0.01	0.01	0.02	0.00	–	0.02	–	–
Na_2O	0.03	0.01	–	0.01	1.29	1.27	0.44	0.38	0.13	0.06	0.04	0.01	–	–	–	0.06
ZnO	–	–	–	–	–	–	–	–	–	–	0.49	0.30	0.56	0.48	–	–
K_2O	0.01	0.08	0.02	0.05	0.02	0.04	8.64	8.46	0.01	–	0.01	0.00	0.01	–	0.02	0.01
F	–	–	–	–	0.33	0.17	0.84	0.42	–	–	–	–	–	–	–	–
Cl	–	–	–	–	–	–	0.01	–			–	–	–	–	–	–
Total	100.94	100.64	100.29	99.87	98.72	98.48	96.16	94.34	100.00	100.54	98.26	98.46	99.01	98.70	98.90	98.62

Cations	12 Ox	12 Ox	12 Ox	12 Ox	23 Ox	23 Ox	22 Ox	22 Ox	18 Ox	18 Ox	23 Ox	23 Ox	4 Ox	4 Ox	3 Ox	3 Ox
Si	2.98	3.01	3.00	3.01	6.88	6.77	5.64	5.61	5.02	5.04	3.54	3.57	0.00	0.00	–	–
Al	1.97	1.97	1.98	1.96	1.94	2.09	2.72	2.74	3.95	3.96	9.06	9.03	1.89	1.88	–	0.01
Fe^{3+}	0.07	–	0.02	0.03	–	–	–	–	–	–	–	–	0.10	0.11	0.14	0.11
Ti	0.00	–	–	–	0.03	0.04	0.38	0.39	–	–	0.11	0.11	–	–	0.93	0.94
Fe^{2+}	1.84	1.89	1.89	1.89	2.76	2.70	1.79	1.78	0.50	0.47	1.33	1.34	0.73	0.73	0.91	0.91
Mn	0.02	0.02	0.02	0.02	0.02	0.01	–	0.01	0.01	–	–	–	–	–	–	–
Mg	1.04	1.04	1.04	1.03	3.26	3.27	3.22	3.24	1.52	1.50	0.73	0.72	0.26	0.25	0.02	0.02
Zn	–	–	–	–	–	–	–	–	–	–	0.05	0.03	0.01	0.01	–	–
Ca	0.07	0.05	0.05	0.05	0.06	0.07	–	0.01	–	–	–	–	–	–	–	–
Na	0.01	–	–	–	0.36	0.36	0.13	0.11	0.03	0.01	0.01	–	0.01	0.01	–	–
K	–	0.01	–	0.01	–	0.01	1.61	1.61	–	–	–	–	–	–	–	–
Total	8.00	7.99	7.99	8.00	15.30	15.32	15.49	15.48	11.02	10.97	14.82	14.80	3.00	3.00	2.00	1.99
X_{Mg}	0.36	0.35	0.35	0.35	0.54	0.55	0.64	0.65	0.75	0.76	0.35	0.35	0.27	0.26	0.02	0.03
%Grs	2.5	1.6	1.7	1.9												
%Alm	62.0	63.2	63.2	63.0												
%Prp	35.1	34.6	34.6	34.5												
% Adr	0.3	–	–	–												
%Sps	0.6	0.6	0.6	0.8												

Additional data available from the first author on request.

from the SHRIMP grain mount (Fig. 10). Some of the analyses of monazite included in garnet are themselves contaminated by micron-scale zircon inclusions, as shown by elevated Zr contents (Table 4). These zircons could not be seen optically but were occasionally observed on the SEM. Correction of the monazite inclusion compositions using the measured Zr contents and average REE compositions of either ~2.69 or ~2.02 Ga zircon showed that contamination had a negligible effect on the REE composition measured for monazite, and therefore uncorrected REE patterns are shown in Fig. 10.

Zircon: Characterization of the full REE patterns for the zircons from the Buick et al. (2003) SHRIMP mount was not possible because of the narrowness of the low Th/U overgrowths which, in order to avoid overlapping of core/overgrowth boundaries, restricted the ablation pit diameter (~20 μm) to be similar to the width of the SHRIMP U–Th–Pb analysis pit. Moreover, because the SHRIMP analysis pits were located where overgrowths were widest, laser ablation pits were situated directly over SHRIMP analysis spots. In general, this resulted in collection of an incomplete dataset for the L-REE to M-REE. Nevertheless, it is evident that although all zircon domains are enriched in the HREE with respect to the MREE, the ~2.69 and ~2.02 Ga zircon populations have significantly different REE patterns (Fig. 11; Table 5). In particular, the high Th/U, ~2.69 Ga zircon cores are characterized by REE patterns of increasing chondrite-normalised abundance from the middle to heavy REE ($Gd_N/Lu_N = 0.04–0.07$) and a pronounced negative Eu anomaly ($Eu/Eu^* = 0.18–0.25$; Fig. 11a). Spots for which LREE data could be collected show $La_N/Gd_N = 0.003–0.027$, and large positive Ce anomalies ($Ce/Ce^* = 5.3$ and 15.8; Table 5). In contrast, the low Th/U, ~2.02 Ga

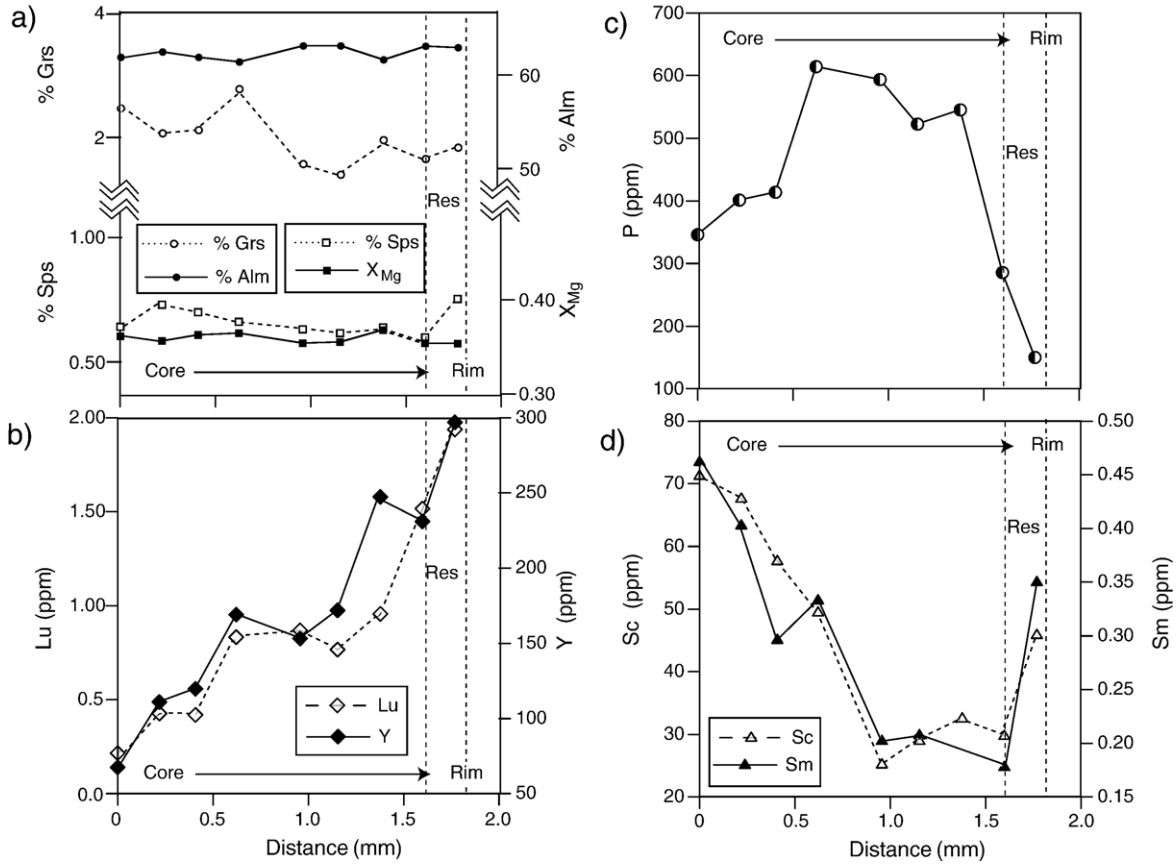

Fig. 9. Major (a), and trace (b, c, d) element core to rim traverse across a garnet in contact with matrix quartz; sample 98 Ma-55. Res = resorbed garnet.

zircon overgrowths (Fig. 11b; Table 5) are characterized by lower REE abundances overall, significantly flatter chondrite-normalised middle to heavy REE patterns

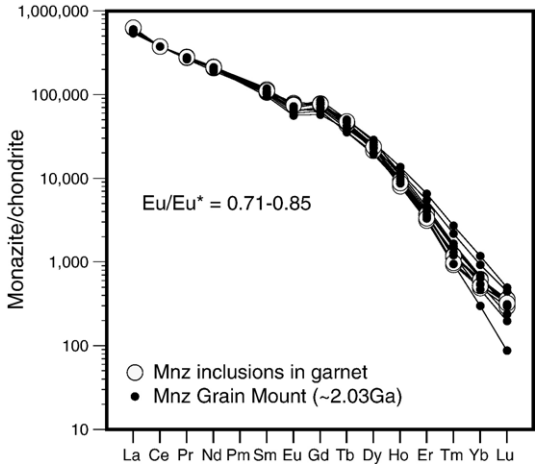

Fig. 10. Chondrite-normalised (Sun and McDonough, 1989) REE data from the monazite SHRIMP mount from sample 98 Ma-55, obtained by LA-ICP-MS. Also shown are REE data obtained in thin section from monazite included in garnet.

(Gd_N/Lu_N = 0.06–0.13), and a very weak negative or positive Eu anomaly (Eu/Eu* = 0.90–1.10). Only one of the two low Th/U ~2.2 Ga zircon overgrowths dated by Buick et al. (2003) could be analysed by LA-ICP-MS. This overgrowth has features intermediate between the two main zircon types; it shows a pronounced negative Eu anomaly (Eu/Eu* = 0.24), similar to the ~2.69 Ga zircon cores, but a somewhat flatter middle to heavy REE pattern (Gd_N/Lu_N = 0.07), similar to some ~2.02 Ga overgrowths, and has Th/U (0.16) intermediate between the two types (Table 5).

Garnet from the core to rim traverse in Fig. 9 is characterised by low (<5–10 ppm) concentrations of Zr and Li, and moderate (10 to 100 s of ppm) concentrations of V, Sc, Y, Ti and P (Table 6). From core to rim, Y (Fig. 9b) and the HREE (shown by Lu in Fig. 9b) contents increase, Zr, Ti and V contents decrease. The P content increases from low values in the core to a zone of high-P concentration intermediate between core and rim; it shows a steep decrease in concentration from this zone to garnet rim (Fig. 9c). Sc and the LREE abundances (Sm in Fig. 9d) initially decrease towards rims to ~1 mm along the traverse, where they show little

Table 4
Laser-ablation trace element data from monazite from the 98 Ma-55 SHRIMP mount and from inclusions in garnet

Element (ppm)	SHRIMP spot							Monazite inclusions in garnet			
	1.1	2.1	3.1	4.1	5.1	6.1	7.1	mnz1*	mnz4*	mnz7*	mnz9*
Li	6.4	5.7	6.3	5.9	6.2	6.4	2.9	6.1	5.9	3.8	6.2
Sc	0.03	0.03	0.00	0.01	0.04	0.02	0.02	0.47	0.63	0.22	1.65
V	2.4	2.4	3.1	3.6	1.6	3.5	1.4	1.4	1.5	1.5	2.4
Sr	37.4	61.7	37.1	40.7	50.2	29.2	79.7	18.3	18.3	40.1	33.7
Y	16,100	18,820	20,635	23,182	18,459	17,727	15,424	14,743	15,262	13,309	14,715
Zr	2.14	2.14	2.06	2.16	3.04	10.94	2.93	149.55	192.78	52.48	426.25
Nb	0.10	0.10	0.11	0.10	0.10	0.08	0.10	0.13	0.14	0.14	0.26
Ba	1025	1032	1035	1025	1025	1046	1071	984	1009	988	1019
La	136,076	137,693	131,618	127,891	131,198	141,470	140,382	147,323	149,096	147,530	148,980
Ce	230,526	230,526	230,526	230,526	230,526	230,526	230,526	230,526	230,526	230,526	230,526
Pr	24,879	25,339	25,925	25,331	25,259	24,505	24,901	25,584	26,052	26,252	25,990
Nd	91,956	95,462	97,088	92,726	95,660	87,589	93,616	94,921	96,482	98,411	97,414
Sm	15,141	17,289	17,736	13,892	15,914	15,692	17,117	15,764	16,535	16,978	16,455
Eu	3533	4001	3969	3138	3489	3608	4037	4297	4471	4317	4206
Gd	13,818	16,949	15,372	11,681	13,674	13,335	15,516	15,191	15,615	14,782	15,331
Tb	1482	1827	1808	1375	1422	1397	1590	1593	1639	1575	1719
Dy	5626	6728	7158	6581	5742	5445	5744	5610	5782	5257	5861
Ho	520	642	586	749	647	553	562	487	512	443	483
Er	568	738	529	1067	888	684	655	579	605	505	539
Tm	28.5	41.3	23.4	68.9	53.3	40.3	37.7	28.2	30.0	23.1	24.4
Yb	71.4	112.6	48.2	196.3	148.8	112.3	111.5	97.4	101.1	79.5	83.3
Lu	4.6	7.78	2.17	12.71	11.20	8.04	8.04	8.31	8.89	7.26	7.98
Hf	0.24	0.23	0.25	0.24	0.21	0.41	0.24	13.91	15.41	10.69	23.15
Ta	0.03	0.04	0.03	0.05	0.03	0.02	0.03	1.15	1.26	1.00	1.17
Pb	809	1947	796	845	1508	654	2918	852	819	1016	858
Th	5032	11851	4768	5243	8346	3464	17512	5517	5457	6690	5703
U	1583	2554	2103	1956	1823	1512	2013	2698	2749	1757	2075
Th/U	3.18	4.64	2.27	2.68	4.58	2.29	8.70	2.05	1.99	3.81	2.75
Eu/Eu*	0.74	0.71	0.73	0.75	0.72	0.76	0.76	0.85	0.85	0.83	0.81
$(La/Gd)_N$	8	7	7	9	8	9	8	8	8	8	8
$(Gd/Lu)_N$	371	269	876	114	151	205	238	226	217	252	238

*=minor zircon contamination.

variation; outwards they increase sharply within ~100 μm of the garnet rim. The latter, near-rim increase mirrors that of Mn (Fig. 9a). Garnet REE patterns (Fig. 12a) are characterised by a steep increase in chondrite-normalised REE abundance from Sm to maximum values at Dy (Sm_N/Dy_N=mostly 0.01–0.05). From core to rim, the REE patterns from Dy to Lu change systematically, from significant relative HREE depletion to relatively flat (Dy_N/Lu_N=6.8 (core) to 1.2 (rim); Fig. 12a). All garnet REE patterns are characterised by small negative to negligible Eu anomalies (Eu/Eu*=0.74–1.02; all but one ≥0.88).

Cordierite is REE-poor (Table 6) with all REE below the LA-ICP-MS detection limits of ~0.005–0.05 ppm for this mineral, and consistent with other studies (for example, Bea et al., 1994). With the exception of Li and P, which locally have concentrations as high as 120–150 ppm, most other trace elements have only low abundances (<1–10 ppm). Of the minerals analysed, cordierite is the only significant sink for Be (~9–15 ppm).

Biotite is characterised by low (<10 ppm) concentrations of Zr, Y and Li, moderate (10 to 100 s ppm) concentrations of Nb, P, Rb, and V, and high (1000 s ppm) Ba contents (Table 6). It shows chondrite-normalised REE profiles characterised by low overall abundances, weak enrichment of the LREE with respect to the MREE, flat MREE and HREE patterns, positive Eu anomalies (Eu/Eu*=1.1–2.05) and variable negative Ce anomalies (Fig. 12b). The low Zr contents (<1–2 ppm) suggest that the biotite does not contain micro-inclusions of zircon. Similarly, the low P contents and overall shape of the chondrite-normalised REE patterns compared to those in Fig. 10 suggests that monazite is not a contaminant. Therefore, the REE patterns are considered to accurately reflect that of biotite itself, rather than contamination by accessory phases.

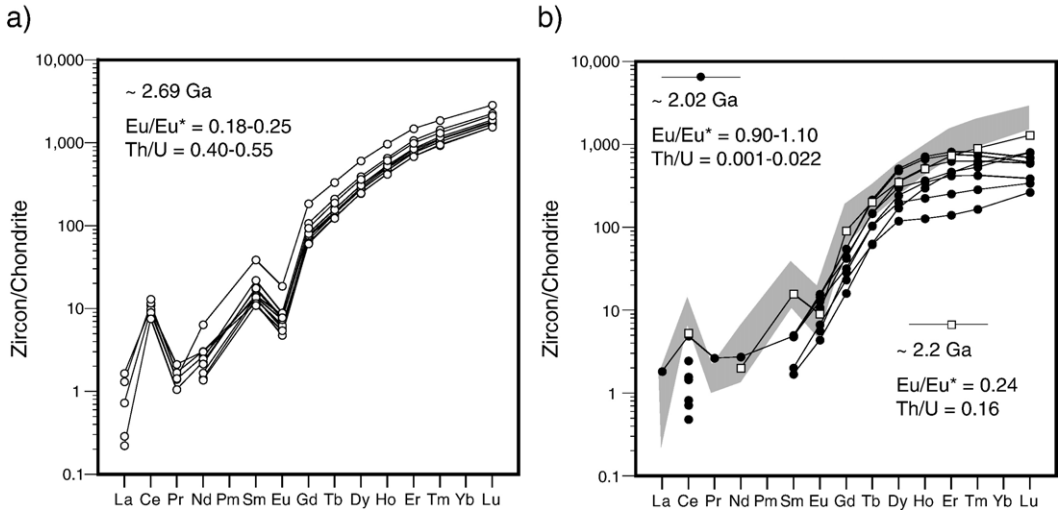

Fig. 11. Chondrite-normalised (Sun and McDonough, 1989) REE data from a) ~2.69 Ga zircon cores; and b) ~2.02 Ga overgrowths and a single ~2.2 Ga zircon overgrowth from the 98 Ma-55 SHRIMP mount of Buick et al. (2003). The shaded field in b) shows the REE patterns of ~2.69 Ga zircon cores for comparison.

Gedrite has moderate concentrations of Li, V, and Y (Table 6). It has asymmetric, convex upward chondrite-normalised REE patterns characterised by low LREE contents that increase (Ce_N/Dy_N=0.01–0.06) to maximum abundances for the M-HREE (Dy to Er; Dy_N/Er_N=0.92–1.01) then decrease slightly from Er to Lu (Er_N/Lu_N=1.54–1.60), and small to moderate positive Eu anomalies (Eu/Eu*=1.09–1.39; Fig. 12c). Although broadly similar in shape to the MREE to HREE patterns obtained from garnet rims, the overall gedrite REE abundances are lower. The steepness in the chondrite-normalised REE pattern from the MREE to LREE for gedrite (Sm_N/Dy_N=0.025–0.035) overlaps with the least steep REE profiles obtained from garnet.

5. Discussion

5.1. Metamorphic conditions

Fe–Mg exchange geothermometry using matrix biotite defining the foliation and garnet compositions taken along the traverse in Fig. 9 yields temperature estimates of ~790–810 °C for an assumed pressure range of 8–10 kbar (consistent with previous thermobarometry in the Central Zone) using the Holdaway et al. (1997) calibration of the garnet–biotite thermometer. Because of the lack of zoning in X_{Mg} shown in garnet along this traverse (chosen because no Fe–Mg phases were in contact with the garnet rim), these temperatures are insensitive to position of the garnet analysis along the traverse and are assumed to be minimum values. Somewhat lower temperatures (~720–760 °C) were returned by garnet–cordierite Fe–Mg exchange thermometry (Nichols et al., 1992) over the same pressure interval using the composition of cordierite in annealed polycrystalline aggregates elongate within the fabric. The temperature estimates overlap with, but are in general slightly lower than, likely estimated peak–metamorphic conditions in the Central Zone. The lack of plagioclase in 98 Ma-55 precludes the use of net-transfer reactions to constrain pressures.

A detailed mineral texture description of 98 Ma-55 is beyond the scope of this study. However, it suffices to note that the embayment of garnet to form cordierite, and sillimanite to form cordierite+spinel-bearing assemblages, as observed in 98 Ma-55 (Fig. 5) is similar to mineral textures described in feldspar-bearing metapelites throughout the Central Zone (e.g., Watkeys, 1984; Zeh et al., 2004), and is consistent with a post-peak metamorphic retrograde evolution characterised by a component of decompression.

5.2. Trace element zoning in garnet

Major element profiles through the garnet in Fig. 9a do not display significant zoning and are likely to have been reset by volume diffusion. The exception to this occurs in the outermost rims, which show slightly higher X_{Sps}, (Fig. 9a), consistent with incipient garnet resorption (Tracy, 1982). In contrast to the lack of major element zonation, the garnet is strongly zoned in trace elements. In particular, from core to rim, Y and HREE contents generally increase (Fig. 9b). P shows an

Table 5
Laser-ablation trace element data from zircon from the 98 Ma-55 SHRIMP mount of Buick et al. (2003)

	~2.69 Ga										~2.2 Ga	~2.02 Ga							
Spot	1.1	2.1	3.2	5.1	7.1	17.1	19.1	20.1	21.1	22.1	16.1	3.1	3.3	8.1	8.2	14.1	23.1	25.1	27.1
Age, Ma	2692 ± 22	2696 ± 15	2666 ± 17	2718 ± 13	2686 ± 13	2691 ± 14	2882 ± 9	2684 ± 12	2651 ± 15	2708 ± 9	2193 ± 14	2027 ± 28	2020 ± 17	1988 ± 17	2029 ± 25	2033 ± 20	1856 ± 8	2034 ± 10	2018 ± 12
(ppm)																			
P	280	250	289	236	269	258	329	292	236	330	449	1356	1433	850	839	569	520	735	619
Sc	264	262	266	288	269	266	277	248	261	263	299	316	317	364	361	388	656	706	477
Ti	4.05	4.13	4.37	4.44	4.03	4.24	4.07	3.66	4.30	4.06	3.37	3.16	3.30	4.39	3.27	3.46	3.57	3.35	4.00
V	bdl	bdl	0.12	bdl	bdl	bdl	bdl	bdl	bdl	bdl	bdl	bdl	bdl	bdl	bdl	bdl	bdl	0.09	bdl
Sr	0.24	0.20	0.20	0.30	0.17	0.19	0.25	0.31	0.19	0.24	0.21	0.14	0.17	0.29	0.30	0.14	0.25	0.17	0.58
Y	734	734	792	766	817	656	1024	1495	658	950	857	1529	1630	1173	778	537	279	650	750
Nb	4.21	3.90	2.99	3.45	4.47	3.42	4.87	2.36	3.13	5.16	1.34	0.29	0.26	0.36	0.30	0.35	2.32	6.48	2.62
Ba	bdl	bdl	0.03	bdl	bdl	bdl	bdl	bdl	bdl	bdl	bdl	bdl	bdl	2.25	0.84	bdl	0.65	bdl	bdl
La	0.31	bdl	0.05	0.17	bdl	0.39	bdl	bdl	bdl	bdl	bdl	bdl	bdl	bdl	0.43	bdl	bdl	bdl	bdl
Ce	7.00	5.83	4.68	5.77	6.70	6.08	7.11	5.50	4.64	7.96	3.10	0.89	0.96	1.49	2.98	0.29	0.50	0.44	0.96
Pr	0.16	bdl	0.10	0.13	bdl	0.20	bdl	0.13	bdl	bdl	bdl	bdl	bdl	bdl	0.25	bdl	bdl	bdl	bdl
Nd	1.40	0.66	1.03	1.21	0.76	1.38	1.13	2.91	0.63	0.99	0.87	bdl	bdl	bdl	1.25	bdl	bdl	bdl	bdl
Sm	1.96	1.90	2.53	2.13	2.02	1.71	3.26	5.75	1.61	2.61	2.22	0.74	0.70	bdl	0.72	bdl	bdl	bdl	0.70
Eu	0.33	0.35	0.43	0.47	0.41	0.27	0.50	1.04	0.30	0.44	0.48	0.86	0.81	0.60	0.72	0.32	0.38	0.25	0.88
Gd	14.5	13.3	16.2	15.2	16.0	12.4	21.2	36.8	12.0	18.6	17.2	10.9	10.9	8.81	6.32	5.69	4.60	3.18	8.42
Tb	4.99	5.01	5.69	5.21	5.65	4.55	7.57	11.99	4.43	6.79	6.98	7.34	7.79	5.29	3.77	3.72	2.24	2.29	5.32
Dy	66.8	67.1	75.0	70.3	76.0	60.3	96.5	149.6	60.6	89.2	82.6	118	125.3	88.1	59.3	49.1	29.2	42.0	73.7
Ho	25.2	25.3	27.9	26.8	28.9	23.0	35.8	52.9	22.7	33.2	26.6	36.4	39.0	28.7	18.9	12.2	6.9	16.3	20.1
Er	121	122	132	124	135	109	171	238	109	158	112	120	130.6	99.9	66.5	40.4	22.4	72.9	74.9
Tm	25.2	25.3	27.6	26.9	29.0	23.0	35.3	46.2	23.3	32.6	21.2	18.0	19.8	15.5	10.4	7.0	4.1	14.6	13.2
Lu	41.3	41.7	44.3	43.3	46.5	37.9	54.9	70.1	38.3	52.5	30.4	14.9	17.0	14.6	9.5	8.4	6.5	19.8	19.6
Hf	9265	9039	8250	9543	9238	8865	9342	8342	8588	9019	10,059	11,748	11,682	11,648	12,123	12,339	13,087	13,578	12,499
Ta	1.87	1.66	1.28	1.55	1.83	1.49	2.11	1.12	1.35	2.23	0.57	bdl	bdl	bdl	0.17	0.36	3.07	9.24	2.71
Pb	16.4	15.5	16.3	12.8	16.8	14.2	22.8	26.4	13.6	25.9	12.2	bdl	bdl	bdl	0.34	bdl	1.05	0.11	2.86
Th	55.4	54.4	57.2	49.6	61.0	47.7	86.0	87.2	46.1	90.8	40.1	0.40	0.46	0.39	0.69	0.72	1.30	0.40	9.28
U	137	132	123	120	149	117	187	158	113	190	244	174	177	280	125	217	287	280	428
Th/U	0.40	0.41	0.46	0.41	0.41	0.41	0.46	0.55	0.41	0.48	0.16	0.002	0.003	0.001	0.005	0.003	0.005	0.001	0.022
Eu/Eu*	0.19	0.21	0.20	0.25	0.22	0.18	0.18	0.22	0.21	0.19	0.24	0.93	0.90		1.03				1.10
Ce/Ce*	7.6		15.8	9.4		5.3									2.2				
$(La/Gd)_N$	0.02		0.003	0.01		0.03									0.06				
$(Gd/Lu)_N$	0.04	0.04	0.05	0.04	0.04	0.04	0.05	0.06	0.04	0.04	0.07	0.09	0.08	0.07	0.08	0.08	0.09	0.02	0.05

Grain numbers refer to the SHRIMP analysis spots from that study.
bdl = below detection limits.

Table 6
Representative trace element (LA-ICPMS) data for major silicate minerals from sample 98 Ma-55

	Grt core	Grt mid	Grt near rim	Grt rim	Ged matrix	Ged matrix	Bt matrix	Bt matrix	Crd matrix	Crd matrix
Concentration (ppm)										
Li	5.1	9.2	6.9	3.5	51	52	7.6	9.1	42	31
P	359	625	295	150	478	482	216	372	21	22
Sc	73	26	30	46	21	24	12	13	0.60	0.47
Ti	147	46	34	52	2680	2781	16,924	18,494	73	7.4
V	100	56	39	34	335	361	495	546	2.9	bdl
Rb	bdl	bdl	bdl	bdl	0.14	0.20	238	247	1.1	bdl
Sr	bdl	bdl	bdl	0.03	9.91	12	18	17	0.82	0.79
Y	66	155	235	297	75	91	2.6	3.7	0.18	bdl
Zr	4.3	3.5	2.2	1.4	5.0	6.5	1.2	0.99	0.20	bdl
Nb	1.2	bdl	bdl	bdl	5.8	6.7	55.3	59.7	0.24	bdl
Cs	bdl	bdl	bdl	bdl	bdl	bdl	1.1	1.2	0.16	0.20
Ba	bdl	bdl	bdl	0.05	0.34	0.36	1172	1214	4.4	1.9
La	bdl	bdl	bdl	bdl	0.13	0.19	1.2	3.6	bdl	bdl
Ce	bdl	0.03	bdl	bdl	0.15	0.23	0.39	1.4	bdl	bdl
Pr	bdl	bdl	bdl	bdl	0.04	0.07	0.29	0.69	bdl	bdl
Nd	bdl	bdl	bdl	bdl	0.28	0.40	1.0	2.6	bdl	bdl
Sm	0.38	0.19	0.18	0.35	0.38	0.69	0.14	0.30	bdl	bdl
Eu	0.51	0.25	0.27	0.38	0.34	0.42	0.07	0.11	bdl	bdl
Gd	8.2	3.3	3.7	3.7	1.8	2.0	0.25	0.35	bdl	bdl
Tb	2.6	1.9	2.3	2.2	0.77	0.94	0.04	0.06	bdl	bdl
Dy	13	19	28	31	8.9	11	0.31	0.51	0.03	bdl
Ho	1.3	4.0	6.4	8.0	2.3	2.8	0.07	0.10	bdl	bdl
Er	1.9	9.5	17	23	7.1	8.1	0.15	0.30	bdl	bdl
Tm	0.19	1.2	2.1	2.9	1.0	1.2	0.02	0.04	bdl	bdl
Yb	1.2	7.0	12	17	6.0	6.3	0.16	0.28	0.02	bdl
Lu	0.15	0.89	1.5	1.9	0.72	0.81	0.02	bdl	bdl	bdl
Hf	0.09	0.09	bdl	bdl	0.54	0.76	0.06	bdl	bdl	bdl
Ta	0.06	bdl	bdl	bdl	0.40	0.44	3.65	3.87	bdl	bdl
Pb	0.38	0.70	0.09	1.4	2.0	1.4	20	20	0.12	0.18
Th	bdl	bdl	bdl	bdl	bdl	bdl	bdl	bdl	bdl	bdl
U	bdl	bdl	bdl	bdl	bdl	bdl	bdl	bdl	bdl	bdl
Eu/Eu*	0.88	0.94	1.0	1.0	1.3	1.1	1.2	1.0		
$(La/Gd)_N$					0.06	0.08	4.0	8.5		
$(Gd/Lu)_N$	6.7	0.45	0.30	0.23	0.30	0.30	1.3			

Additional data available from the first author on request.
bdl = below detection limits.

initial rimwards enrichment until ~0.6 mm from the core (Fig. 9c), before being lowered across a ~1 mm zone toward the garnet rim. Sc and the L-MREE (Fig. 9d) decrease from the core to approximately ~1 mm along the traverse, after which they show near constant values until close to the rim.

The core to rim increase in Y and the HREE is the opposite trend to the decrease commonly observed in high-grade garnets in metapelitic rocks, and which is interpreted as reflecting fractionation processes during garnet growth (cf., Pyle and Spear, 1999; Otamendi et al., 2002). It is also opposite to the trend observed in metapelites where garnet has grown in equilibrium with monazite through reactions involving apatite and plagioclase (Pyle et al., 2001; Yang and Rivers, 2002). The origin of the compositional trends, and in particular the enrichment of Y and the HREE in the garnet from 98 Ma-55 is problematic. Normal (plagioclase-bearing) amphibolite-facies metapelitic rocks garnets, which overall show core to rim decreases in Y and the HREE (Pyle and Spear, 1999; Yang and Rivers, 2002), commonly also show mid-grain annuli of Y enrichment. These have been inferred to reflect prograde garnet resorption between several growth episodes (Pyle and Spear, 1999; Yang and Rivers, 2002; Kohn and Malloy, 2004). Partial resorption of garnet during retrogression may also result in preferential enrichment of Y and the HREE in garnet rims (Pyle and Spear, 1999; Yang and Rivers, 2002; Storkey et al., 2005). Pyle and Spear (1999) invoked dissolution of Y- and REE-bearing phosphates during partial melting to explain narrow zones of trace element enrichment in garnets from anatectic metapelites.

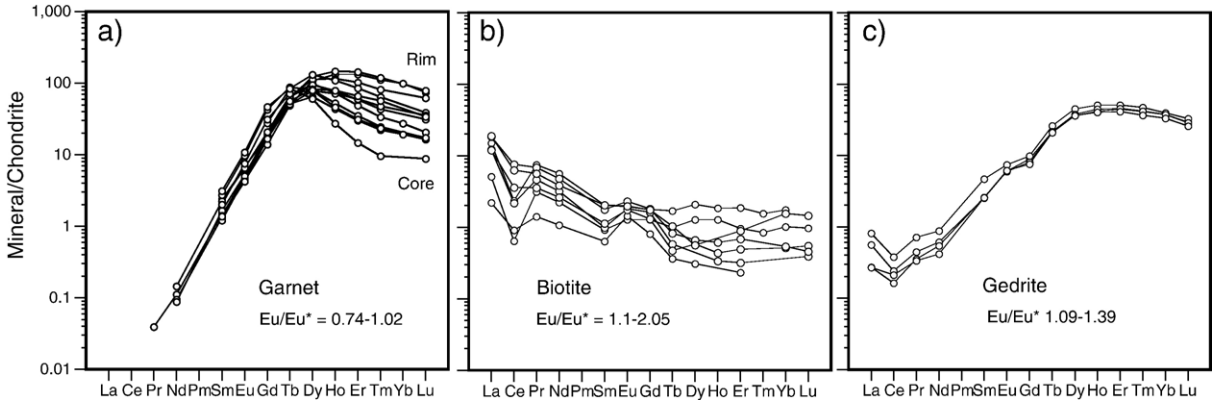

Fig. 12. Chondrite-normalised (Sun and McDonough, 1989) REE data (La-ICP-MS) from garnet, gedrite and biotite from sample 98 Ma-55.

In the present study the garnet grain analysed was chosen because it showed very little evidence of retrograde resorption (Fig. 9a); this process is therefore unlikely to have caused the observed core to near-rim trace element zonation. Similarly, none of the rocks from the present locality show field evidence for having partially melted (Fig. 4), suggesting that melting reactions involving accessory phase dissolution are also unlikely to have released trace elements into garnet. Compared with the monazite–garnet Y partitioning observed in amphibolite-facies metapelites the core to rim variation in the garnet from 98 Ma-55 might indicate that garnet grew during cooling (cf. Pyle et al., 2001; Yang and Rivers, 2002). However, the garnet is wrapped by the peak metamorphic fabric and locally contains staurolite inclusions near its core, suggesting that it grew during prograde metamorphism.

An alternative explanation for the trace element enrichment during garnet growth could involve the sub-solidus breakdown of trace element-rich minerals (Yang and Rivers, 2002). In sample 98 Ma-55 the garnet contains relatively little record of prograde minerals. Staurolite and allanite are the only minerals found as inclusions in garnet cores that do not also occur in the rock matrix. Staurolite was not analysed because it is typically has extremely low (sub-ppm) Y and REE contents (Pyle et al., 2001; Buick, unpublished data). Monazite in 98 Ma-55 occurs in the matrix, and in mid-to-rim positions in garnet, but not in garnet cores. Rare textural relationships suggest that monazite partially replaced allanite, but such a reaction relationship additionally requires a source of phosphorus. This in turn suggests that, prior to garnet growth, 98 Ma-55 may have contained phosphate minerals such as xenotime or apatite and that these phases were exhausted during prograde metamorphism. We propose the following reaction to explain some of the key-features of the trace element geochemistry of garnet in 98 Ma-55:

$$\text{Allanite} + \text{Xenotime} + \text{Sillimanite} = \text{Monazite} + \text{Garnet} + \text{Quartz} + H_2O \quad (1)$$

$$\text{LREECaFeAl}_2\text{Si}_3\text{O}_{12}(\text{OH}) + (\text{Y},\text{HREE})\text{PO}_4 + 0.5\text{Al}_2\text{SiO}_5 = \text{LREEPO}_4 + (\text{Y},\text{HREE})\text{CaFeAl}_2(\text{AlSi}_2)\text{O}_{12} + 1.5\text{SiO}_2 + 0.5\text{H}_2\text{O}$$

As most of the involved phases are solid solutions, this is a continuous reaction that would be able to produce an increase in Y and HREE in garnet during prograde garnet growth until xenotime is consumed. Also it is in agreement with the textural observation that there are allanite relics in the core of garnet and that the onset of monazite formation occurs in the intermediate part of the garnet where Y and HREE increase. However, in detail there is more complexity. In particular, P zonation is more complicated. P might be incorporated in garnet either by a coupled substitution:

$$M^{1+}P \leftrightarrow M^{2+}Si \text{ or } M^{3+}P \leftrightarrow 2Si,$$

and hence it is unlikely that a simple buffering relationship can be formulated.

At the outermost rim, all trace elements compatible in garnet significantly increase. The near-rim increases are coincident with that of Mn (Fig. 9a) and probably reflect preferential retention in garnet during incipient resorption (cf., Hermann and Rubatto, 2003; Storkey et al., 2005). This trend may be partially masked for Y and the HREE (Fig. 9b) by their overall rimward increase in concentration. A polyphase garnet growth history generally is associated with significant spikes in Y and HREE in core rim traverses due to partial garnet

resorption prior to new growth (Pyle and Spear, 1999). Also, garnet of different grain size is likely to form in a polyphase evolution (Hermann and Rubatto, 2003). Such features have not been observed in the investigated rocks. Therefore, we interpret the garnet has having most likely grown during a single high-grade metamorphic event. It is worth noting that garnet lacks a negative Eu-anomaly from core to rim, indicating that it grew in the absence of plagioclase.

5.3. Timing of metamorphism

The new SHRIMP monazite U–Pb analyses presented here yield a mean weighted ^{207}Pb–^{206}Pb age of 2028 ± 3 Ma, and support the interpretation of Buick et al. (2003) that high-grade metamorphism at this locality occurred during the Palaeoproterozoic. Although no monazite U–Pb data were collected in thin section, the tight cluster of REE data obtained from monazite included in poikiloblastic garnet fall within the range of monazite compositions determined on the SHRMP mount. In particular, the steep depletion in HREE and the small negative Eu anomaly suggest that the monazite inclusions also formed during the same 2.03 Ga event. Despite, this and because monazite does not occur in garnet cores it is possible that the garnet had an earlier growth history, either: a) at ~2.7–2.5 Ga, as recorded elsewhere in the Central Zone (Holzer et al., 1998); b) at ~2.2 Ga, as suggested by the rare zircon overgrowths dated by Buick et al. (2003); or c) under amphibolite-facies conditions during prograde ~2.03 Ga metamorphism. There is no evidence of ~2.7–2.5 Ga metamorphic zircon or monazite in 98 Ma-55, and therefore the first possibility is unlikely. The ~2.2 Ga zircon analyses have ages and a single trace element composition intermediate between ~2.69 Ga igneous and ~2.02 Ga metamorphic zircon, suggesting a mixed analysis. Moreover, there is no evidence of metamorphism or magmatism in the Central Zone in the interval ~2.50–2.05 Ga (Egglington and Armstrong, 2004). Additionally, the trace element profiles in garnet do not provide support for such a polyphase evolution, and hence we suggest that garnet formed during prograde metamorphism from amphibolite to granulite facies in a tectonometamorphic event at ~2.03 Ga.

Textural and trace element relationships observed in thin section indicate that in 98 Ma-55 both zircon and monazite formed no later than the development of the peak-metamorphic assemblage (Figs 6, 8b). These include: 1) the occurrence of both phases aligned within inclusion fabrics in peak-metamorphic garnet; 2) the similarity between the REE patterns in included monazite and those in dated ~2.03 Ga monazite from the SHRIMP mount; 3) the high abundance of micron-sized zircon in clusters with monazite in garnet—this zircon is clearly texturally different from the relatively coarse grained, prismatic, ~2.69 Ga zircon dated in the SHRIMP grain mount; 4) the occurrence of distinct overgrowths on inferred ~2.69 Ga zircon included in garnet; and 5) mutual inclusion of monazite and zircon grains that are themselves included in garnet.

Direct textural evidence that can be used to infer the reactions that controlled the growth of monazite and zircon are rare. Locally, there is textural evidence that monazite grew at the expense of early allanite. We suggest that reaction (1) was partly responsible for monazite growth. Alternatively, monazite can form as reaction product of allanite + apatite. While it is possible that monazite formed through both allanite- and apatite-consuming reactions (cf., Smith and Barreiro, 1990), apatite was not observed in the rest of the rock outside of the ~2.69 Ga zircon and therefore there is no direct evidence to support the involvement of apatite as a reactant in the monazite-forming reaction. The occurrence of abundant micron-scale zircon inclusions in garnet that are texturally distinct from the much coarser prismatic ~2.69 Ga zircon suggests that the former did not form by solid-state recrystallisation of ~2.69 Ga zircon. Coarser zircon inclusions in garnet preserve cores and narrow overgrowths that are very similar in CL response to the ~2.69 Ga igneous zircon and ~2.02 Ga metamorphic zircon overgrowths, respectively, in the zircon grain mount (Fig. 8). Given their occurrence as inclusions in garnet it is unlikely that the zircon overgrowths formed through late crystallisation of partial melt. Whether silicate minerals were involved in zircon formation (Fraser et al., 1997) remains unclear; none of the silicate minerals in the peak-metamorphic assemblage contain appreciable (>50–100 ppm) Zr, and most have ≤5 ppm (Table 6). Ilmenite and rutile, which occur as inclusions in the garnet and in the matrix, have been shown in previous studies to contain appreciable Zr contents (100 to 1000 s ppm; Bingen et al., 2001; Zack et al., 2004). However, unlike Bingen et al. (2001), in the present study no textural relationships were observed between new zircon and reactant ilmenite or rutile. Moreover, the Zr contents of rutile in equilibrium with zircon and quartz increase with increasing temperature (Zack et al., 2004), and textural evidence suggests that magmatic ilmenite may exsolve Zr-rich minerals during cooling (Bingen et al., 2001). These observations suggest that it is unlikely that that ilmenite or rutile liberated Zr to form new zircon during prograde or peak metamorphic conditions in this study.

To relate the ages obtained from in situ U–Pb geochronology of accessory phases to metamorphic histories characterised primarily by garnet (as the most useful *P–T*-sensitive mineral and REE carrier), it is necessary to know how trace elements partition between these phases in rocks with relatively simple metamorphic histories. There are relatively few empirical studies where this has been attempted (Pyle and Spear, 1999; Pyle et al., 2001; Rubatto, 2002; Hermann and Rubatto, 2003; Pyle and Spear, 2003; Whitehouse and Platt, 2003; Hokada and Harley, 2004; Kelly and Harley, 2005). Textural evidence suggests that monazite and zircon growth in sample 98 Ma-55 occurred pre- to syn-the metamorphic peak. Because garnet strongly partitions the HREE, syn-garnet growth is also generally consistent with steep depletion in the HREE exhibited by ~2.03 Ga monazite (Fig. 10) and the flatter MREE profiles in the ~2.02 Ga zircon overgrowths than in the ~2.69 Ga zircon cores (Fig. 11).

REE partitioning between an average composition of ~2.03 Ga monazite (SHRIMP mount), coeval low Th/U zircon overgrowths and garnet taken at three points along the traverse in Fig. 9 (core; midway along the traverse and just inboard from the resorbed rim) are shown in Fig. 13. Apparent REE partition coefficients between monazite and zircon decrease monotonically from La to Lu (Fig. 13a). The REE partition preferentially into monazite for all REE except Lu ($K_d \approx 0.6$). These coefficients are very similar to those determined from coeval monazite and metamorphic zircon by Hermann and Rubatto (2003). REE partitioning between the ~2.03 Ga monazite and garnet (Fig. 13b) is harder to determine because the garnet composition varies along the traverse. Coefficients calculated using garnet from mid traverse or near-rim positions decrease monotonically from Sm to Lu (Fig. 13b) and are similar to the partitioning found by Hermann and Rubatto (2003). In contrast, partitioning calculated using the garnet core composition is characterised by an inflection in the profile at Tb, with partitioning from Tb to Lu favouring monazite much more than found by Hermann and Rubatto (2003). Monazite was not observed in garnet cores in 98 Ma-55, so it is likely that the coefficients determined from the garnet core composition are erroneous. The coefficients calculated using garnet outside the core (Fig. 13b) favour monazite over garnet slightly more for the middle to heavy REE than those obtained by Hermann and Rubatto (2003). The REE consistently partition preferentially into monazite relative to garnet from Sm ($K_d \approx 80{,}000$–$90{,}000$) to Lu ($K_d \approx 5$–9). Given that monazite inclusions are not restricted to garnet rims it is not possible to differentiate between

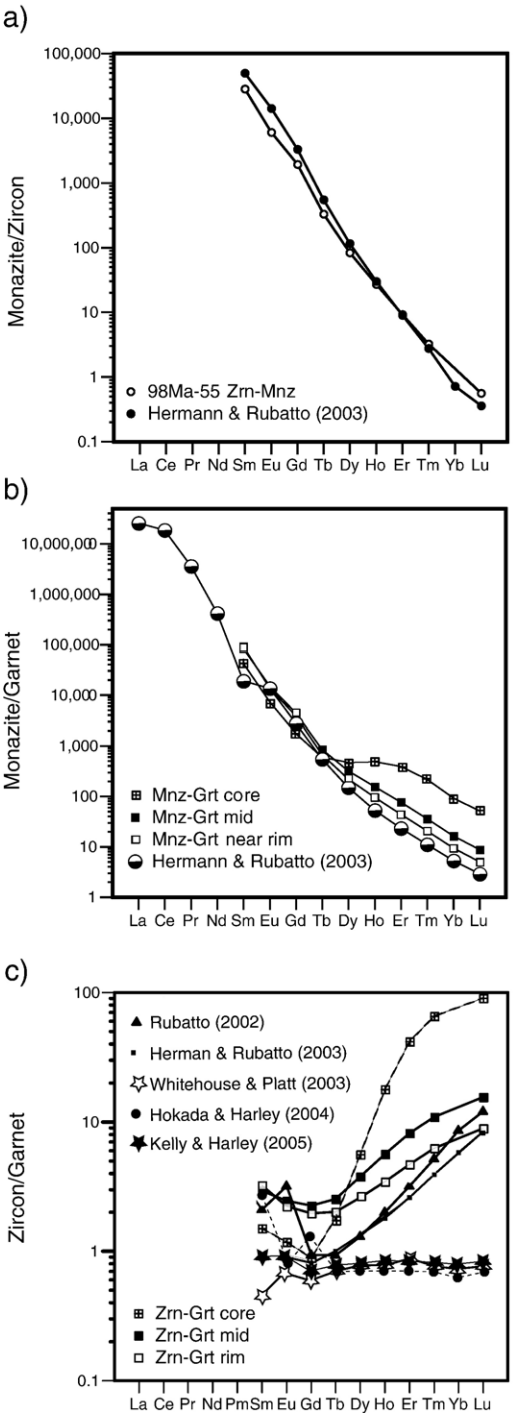

Fig. 13. Apparent REE partition coefficients between garnet, ~2.02 Ga zircon and ~2.03 Ga monazite from sample 98 Ma-55. Garnet REE data were taken from the core of the traverse in Fig. 9, at a position intermediate between core and rim and just inboard from the garnet rim. Empirical determined partitioning from Rubatto (2002), Hermann and Rubatto (2003), Whitehouse and Platt (2003), Hokada and Harley (2004) and Kelly and Harley (2005) are shown for comparison.

estimates based on garnet analyses from mid- and near-rim positions.

Apparent partitioning coefficients between the ~2.02 Ga zircon and garnet are shown in Fig. 13c. As with the case of monazite–garnet partitioning, the partition coefficients calculated using the garnet core favour zircon over garnet for the HREE ($^{Lu}K_{d\ Zrn/Grt} \approx 90$) much more than is indicated by any previous study, and are not likely to represent an equilibrium partitioning. In contrast, partitioning calculated using either of the other two garnet compositions resulted in similar partition coefficients of ~2–3 between Sm and Tb, and more divergence from Tb to Lu ($^{Lu}K_{d\ Zrn/Grt} \approx 9$–16; Fig. 13c). Partitioning coefficients calculated using the garnet near-rim composition are closest to those calculated by Hermann and Rubatto (2003) and Rubatto (2002) for zircon and garnet from granulite-facies metapelites. However, they differ significantly from the inferred partitioning of Whitehouse and Platt (2003; granulite-facies metapelite), and from studies of UHT granulites (Hokada and Harley, 2004; Kelly and Harley, 2005), which predict partition coefficients for the HREE that favour garnet over zircon (Fig. 13c). The reasons for this disagreement are unclear, but may potentially include, solely or in combination, a temperature or garnet compositional control of partition coefficients, the effects of self-diffusion on garnet trace element compositional profiles under UHT conditions, or that zircon did not grow at the same time as garnet (cf. Roberts and Finger, 1997). Experimental partitioning studies and more integrated geochronological and trace element studies of garnet and zircon growth in natural systems are required to resolve this problem.

5.4. Origin of the protolith

Cordierite–gedrite– and garnet-bearing rocks from Oom Stammetjie se Kop lack both plagioclase and K-feldspar. The origin of Ca- and Na-poor, cordierite–gedrite rock types is controversial. They have been interpreted to result from a range of pre- and syn-metamorphic processes. These include metamorphism of rocks whose unusual bulk composition resulted from intense chemical weathering during deposition of sedimentary precursors (Moore and Waters, 1990), metamorphism of hydrothermally altered volcano-sedimentary successions (Vallance, 1967), syn-metamorphic hydrothermal alteration (Vry, 1994) and the segregation of partial melt to leave behind refractory residual bulk compositions (Grant, 1968).

The trace element patterns of minerals in 98 Ma-55 place some constraints on when depletion of the "feldspar component" of the rock occurred. In particular, ~2.69 Ga igneous zircons inherited from the protolith show a conspicuous negative Eu anomaly, whereas the ~2.02 Ga zircon overgrowths and garnet preserve either neglible or no Eu anomalies. Negative Eu anomalies in zircon are generally thought to reflect trace element equilibration in the presence of plagioclase and/or K-feldspar, or crystallisation in a magma from which feldspars have been removed by crystal fractionation (Hoskin et al., 2000). In contrast, the lack of an Eu anomaly suggests that feldspars were not present when the zircon formed (Rubatto, 2002). This suggests that in 98 Ma-55 open-system processes affecting feldspars occurred between ~2.69 and ~2.02 Ga i.e.,before the metamorphic peak. Interestingly, not even the garnet core displays a negative Eu anomaly, indicating that the feldspar component must have been removed from the protolith prior to the onset of garnet growth. This rules out an origin of the protolith related to high-grade metamorphic processes such as syn-metamorphic alteration or melt extraction.

It is interesting to note that while there is no significant negative Eu anomaly in any major mineral, bulk rock compositions display a clear negative Eu anomaly. We suggest this negative Eu anomaly is carried by the ~2.69 Ga zircon and included apatite, relict allanite and newly-formed monazite. The small negative Eu anomalies in monazite may have been inherited from precursor minerals via reaction (1).

A detailed discussion of the nature of the processes that caused the pre-metamorphic development of the unusual compositions of the cordierite–orthoamphibole rocks at Oom Stammetjie se Kop is beyond the scope of this contribution. However, it should be noted that regardless of whether the feldspar-breakdown process involved pre-2.03 Ga hydrothermal alteration or intense weathering the terrain must have been either at a shallow (hydrothermal alteration) or surficial crustal level at this time. This has implications for the tectonics of the Central Zone post-2.69 Ga and prior to the burial of the terrain to a depth of ~25–40 km (8–12 kbar) by ~2.03 Ga, and is consistent with a post-2.69 Ga depositional age obtained from a feldspar-bearing Central Zone quartzite by Barton et al. (2003).

6. Conclusions

High-grade feldspar-free, garnet–cordierite–gedrite–biotite-bearing rocks of presumed metasedimentary origin from the Central Zone of the Limpopo Belt (South Africa) have unusual trace element-rich bulk compositions. Garnet from one such sample shows

little major element zoning but significant trace element zonation characterised by core to rim increases in Y and the HREE and decreases in Sc and the LREE, followed by minor increases within ~100 μm of the rim due to incipient garnet resorption. Zoning patterns for Y and the HREE were controlled by the breakdown of accessory phases (allanite and xenotime ± apatite). SHRIMP U–Pb dating of monazite from the same rock suggests that peak metamorphism occurred at 2028 ± 3 Ma, in agreement with a previous SHRIMP age determination of 2022 ± 11 Ma on metamorphic zircon overgrowths from the same sample. Textural evidence suggests that new monazite and zircon growth occurred synchronously with growth of the mid- to outer-rim regions of garnet, thus allowing mineral–mineral partition coefficients to be established. M-HREE partitioning between coeval monazite and zircon overgrowths is similar to that obtained from the only previously published study. HREE are preferentially incorporated in zircon ($^{Lu}K_{d\ Zrn/Grt} \approx 9–16$) and monazite ($^{Lu}K_{d\ Mnz/Grt} \approx 5–9$) with respect to garnet. The geochronological and trace element data are most consistent a single episode of high-grade metamorphism at ~2.03 Ga.

Inherited (or detrital), moderate to high Th/U, 2692 ± 8 Ma igneous zircon from the protolith has a prominent negative Eu anomaly, consistent with zircon precipitation in the presence of feldspar, or in a Eu-depleted environment resulting from prior feldspar fractionation. In contrast, the low Th/U ~2.02 Ga metamorphic zircon overgrowths and garnet lack an Eu anomaly, suggesting that they formed in the absence of feldspar. This suggests that the bulk composition of the precursors to this rock was modified by either open system hydrothermal or weathering reactions that broke down and removed the feldspar component of the rock between ~2.69 and ~2.02 Ga, i.e.,before the metamorphic peak, and requires that the protoliths were at shallow or surficial crustal levels prior to the ~2.03 Ga event.

Acknowledgements

The manuscript benefited from helpful reviews by Ian Fitzsimons and Andreas Möller, and additional comments and editorial handling by Joe Pyle. A. Priymak (University of Melbourne), and C. Allen and M. Shelley (RSES, Australian National University) are thanked for technical assistance. J. Smit and E. Spicer (University of Stellenbosch, South Africa) are thanked for help with the production of whole-rock fused disks for laser ablation. ISB acknowledges support from the Australian Research Council (ARC; Australian Professorial Fellowship and Discovery Grant No. DP0342473). JH and DR acknowledge financial support from the ARC and the Swiss National Science Foundation.

References

Barton Jr., J.M., Holzer, L., Kamber, B.S., Doig, R., Kramers, J.D., Nyfeler, D., 1994. Discrete metamorphic events in the Limpopo Belt, southern Africa, implications for the application of *P–T* paths in complex metamorphic terrains. Geology 22, 1035–1038.

Barton, J.M. Jr., Barnett, W.P., Barton, E.S., Barnett, M., Doorgapershad, A., Twiggs, C., Klemd, R., Martin, J., Mellonig, L., Zenglein, R., 2003. The geology of the area surrounding the Venetia kimberlite pipes, Limpopo Belt, South Africa: a complex interplay of nappe tectonics and granitoid magmatism. S. Afr. J. Geol. 106, 109–128.

Bea, F., Pereira, M.D., Stroh, A., 1994. Mineral/leucosome trace-element partitioning in a peraluminous migmatite (a laser ablation-ICP-MS study). Chem. Geol. 117, 291–312.

Bingen, B., Austrheim, H., Whitehouse, M., 2001. Ilmenite as a source for zirconium during high-grade metamorphism? Textural evidence from the Caledonides of western Norway and implications for zircon geochronology. J. Petrol. 42, 355–375.

Boryta, M.D., Condie, K.C., 1990. Geochemistry and origin of the Archaean Beit Bridge complex, Limpopo Belt, South Africa. J. Geol. Soc. (Lond.) 147, 229–239.

Buick, I.S., Williams, I.S., Gibson, R.L., Cartwright, I., Miller, J.A., 2003. $\delta^{13}C$ and U–Pb evidence for a Palaeoproterozoic crustal component in the Central Zone of the Limpopo Belt, South Africa. J. Geol. Soc. (Lond.) 160, 601–612.

Degeling, H., Eggins, S., Ellis, D., 2001. Zr budgets for metamorphic reactions, and the formation of zircon from garnet breakdown. Mineral. Mag. 65, 749–758.

Egglington, B., Armstrong, R., 2004. The Kaapvaal craton and adjacent orogens, southern Africa: a geochronological database and overview of the geological development of the craton. S. Afr. J. Geol. 107, 13–32.

Fraser, G., Ellis, D., Eggins, S., 1997. Zirconium abundance in granulite-facies minerals with implications for geochronology in high-grade rocks. Geology 25, 607–610.

Grant, J.A., 1968. Partial melting of common rocks as a possible source of cordierite–anthophyllite assemblages. Am. J. Sci. 273, 289–317.

Hermann, J., Rubatto, D., 2003. Relating zircon and monazite domains to garnet growth zones: age and duration of granulite facies metamorphism in the Val Malenco lower crust. J. Metamorph. Geol. 21, 833–852.

Holdaway, M.J., Mukhopadhyay, B., Dyar, M.D., Guidotti, C.V., Dutrow, B.L., 1997. Garnet–biotite geothermometry revised: new Margules parameters and a natural specimen data set from Maine. Am. Mineral. 82, 582–595.

Holzer, L., Frei, R., Barton, J.M., Kramers, J.D., 1998. Unravelling the record of successive high-grade events in the Central Zone of the Limpopo Belt using Pb single phase dating of metamorphic minerals. Precambrian Res. 87, 87–115.

Hokada, T., Harley, S.L., 2004. Zircon growth in UHT leucosome: constraints from zircon–garnet rare earth elements (REE) relations in Napier Complex, east Antarctica. J. Mineral. Petrol. Sci. 99, 180–190.

Hoskin, P.W.O., Black, L.P., 2000. Metamorphic zircon formation by solid-state recrystallization of protolith igneous zircon. J. Metamorph. Geol. 18, 423–439.

Hoskin, P.W.O., Kinny, P.D., Wyborn, D., Chappell, B.W., 2000. Identifying accessory mineral saturation during differentiation in granitoid magmas: an integrated approach. J. Petrol. 41, 1365–1396.

Kelly, N.M., Harley, S.L., 2005. An integrated microtextural and chemical approach to zircon geochronology: refining the Archaean history of the Napier Complex, east Antarctica. Contrib. Mineral. Petrol. 149, 57–84.

Kohn, M.J., Malloy, M.A., 2004. Formation of monazite via prograde metamorphic reactions involving common silicate minerals: implications for age determinations. Geochim. Cosmochim. Acta 68, 101–113.

Košler, J., 2001. Laser-ablation ICPMS study of metamorphic minerals and processes. In: Sylvester P. (Ed.), Laser-Ablation-ICPMS in the Earth Sciences. Principles and Applications, Mineral. Soc. Canada Short Course, vol. 29, pp. 185–202.

Kröner, A., Nemchin, A.A., Jaekel, P., Hofmann, A., Brandl, G., Pidgeon, R.T., 1998. Field relationships and age of supracrustal Beit Bridge Complex and associated granitoid gneisses of the Central Zone of the Limpopo Belt, South Africa. S. Afr. J. Geol. 101, 201–213.

Kröner, A., Jaekel, P., Brandl, G., Nemchin, A.A., Pidgeon, R.T., 1999. Single zircon ages for granitoid gneisses in the Central Zone of the Limpopo Belt, southern Africa and geodynamic implications. Precambrian Res. 93, 299–337.

Leake, B.E., Woolley, A.R., Arps, C.E.S., Birch, W.D., Gilbert, M.C., Grice, J.D., Hawthorne, F.C., Kato, A., Kisch, H.J., Krivovichev, V.G., Linthout, K., Laird, J., Mandarino, J.A., Maresch, W.V., Nickel, E.H., Rock, N.M.S., Schumacher, J.C., Smith, D.C., Stephenson, N.C.N., Ungaretti, L., Whittaker, E.J.W., Youzhi, G., 1997. Nomenclature of amphiboles: report of the Subcommittee on Amphiboles of the International Mineralogical Association, Commission on New Minerals and Mineral Names. Mineral. Mag. 61, 295–321.

McDonough, W.F., Sun, S.-s., 1995. The composition of the Earth. Chem. Geol. 120, 223–253.

Moore, J.M., Waters, D.J., 1990. Geochemistry and origin of cordierite–orthoamphibole/orthopyroxene–phlogopite rocks from Namaqualand, South Africa. Chem. Geol. 85, 77–100.

Nichols, G.I., Berry, R.F., Green, D.H., 1992. Internally consistent gahnitic–spinel–cordierite–garnet equilibria in the FMASHZn system: geothermobarometry and applications. Contrib. Mineral. Petrol. 111, 362–377.

Otamendi, J.E., de la Rosa, J.D., Patiño Douce, A.E., Castro, A., 2002. Rayleigh fractionation of heavy rare earths and yttrium during metamorphic garnet growth. Geology 30, 159–162.

Pearce, N.J.G., Perkins, W.T., Westgate, J.A., Gorton, M.P., Jackson, S.E., Neal, C.R., Chenery, SP., 1997. A compilation of new and published major and trace element data for NIST SRM 610 and NIST SRM 612 glass reference materials. Geostand. Newsl. 21, 115–144.

Pyle, J.M., Spear, F.S., 1999. Yttrium zoning in garnet: coupling of major and accessory phases during metamorphic reactions. Geol. Mat. Res. 1, 1–49.

Pyle, J.M., Spear, F.S., 2003. Four generations of accessory-phase growth in low-pressure migmatites from SW New Hampshire. Am. Mineral. 88, 338–351.

Pyle, J.M., Spear, F.S., Rudnick, R.L., McDonough, W.F., 2001. Monazite–xenotime–garnet equilibrium in metapelites and a new monazite–garnet thermometer. J. Petrol. 42, 2083–2107.

Roberts, M.P., Finger, F., 1997. Do U–Pb zircon ages from granulites reflect peak metamorphic conditions? Geology 25, 319–322.

Roering, C., van Reenen, D.D., Smit, C.A., Barton, J.M., de Beer, J.H., de Wit, M.J., Strettler, E.H., van Schalkwyk, J.F., Stevens, G., Pretorius, S., 1992. Tectonic model for the Limpopo Belt. Precambrian Res. 55, 539–552.

Rubatto, D., 2002. Zircon trace element geochemistry: partitioning with garnet and the link between U–Pb ages and metamorphism. Chem. Geol. 184, 123–138.

Smith, H.A., Barreiro, B., 1990. Monazite U–Pb dating of staurolite grade metamorphism in pelitic schists. Contrib. Mineral. Petrol. 105, 602–615.

Steiger, R.H., Jäger, E., 1977. Subcommission on geochronology: convention on the use of decay constants in geo- and cosmochronology. Earth Planet. Sci. Lett. 36, 359–362.

Storkey, A., Hermann, J., Hand, M., Buick, I.S., 2005. Using in situ trace element determinations to monitor partial melting processes in metabasites. J. Petrol. 46, 1283–1308.

Sun, S.-s., McDonough, W.F., 1989. Chemical and isotopic systematics of oceanic basalts: implications for mantle composition and processes. In: Saunders Jr., A.D., Norry, M.J. (Eds.), Magmatism in the Ocean Basins, Geol. Soc. Lond. Spec. Pub., vol. 42, pp. 313–345.

Tracy, R.J., 1982. Compositional zoning and inclusions in metamorphic minerals. In: Ferry, J.M. (Ed.), Characterization of Metamorphism through Mineral Equilibria, Rev. Mineral., vol. 10, pp. 355–397.

Vallance, T.G., 1967. Mafic rock alteration and isochemical development of some cordierite–anthophyllite rocks. J. Petrol. 8, 84–96.

Van Orman, J.A., Grove, T.L., Shimizu, N., Layne, G.D., 2002. Rare earth element diffusion in a natural pyrope single crystal at 2.8 GPa. Contrib. Mineral. Petrol. 142, 416–424.

Vry, J., 1994. Boron-free kornerupine from the Reynolds Range, Arunta Block, central Australia. Mineral. Mag. 58, 27–37.

Watkeys, M.K., 1984. The Precambrian geology of the Limpopo Belt north and west of Messina. Unpublished Ph D. thesis, University of the Witwatersrand, Johannesburg.

Whitehouse, M.J., Platt, J.P., 2003. Dating high-grade metamorphism—constraints from rare-earth elements in zircon and garnet. Contrib. Mineral. Petrol. 145, 61–74.

Williams, I.S., Claesson, S., 1987. Isotopic evidence for the provenance and Caledonian metamorphism of high grade paragneisses from the Seve Nappes, Scandinavian Caledonides. Ion microprobe zircon U–Th–Pb. Contrib. Mineral. Petrol. 97, 205–217.

Williams, I.S., Buick, I.S., Cartwright, I., 1996. An extended episode of Early Mesoproterozoic metamorphic fluid flow in the Reynolds Range, central Australia. J. Metamorph. Geol. 14, 29–47.

Yang, P., Rivers, T., 2002. The origin of Mn and Y annuli in garnet and the thermal dependence of P in garnet and Y in apatite in calc-pelite and pelite, Gagnon terrane, western Labrador. Geol. Mat. Res. 4, 1–35.

Zack, T., Moreas, R., Kronz, A., 2004. Temperature dependence of Zr in rutile: calibration of a rutile thermometer. Contrib. Mineral. Petrol. 148, 471–488.

Zeh, A., Klemd, R., Buhlmann, S., Barton, J.M., 2004. Pro- and retrograde *P–T* evolution of granulites of the Beit Bridge Complex (Limpopo Belt, South Africa): constraints from quantitative phase diagrams and geotectonic implications. J. Metamorph. Geol. 22, 79–95.